Dual Use of Liquid Hydrogen in a Next-Generation PEMFC-Powered Regional Aircraft With Superconducting Propulsion

Christian Hartmann, Jonas Kristiansen Nøland, *Senior Member, IEEE*, Robert Nilssen, and Runar Mellerud

***Abstract*— In this article, we present a comprehensive model framework for a disruptive cryoelectric propulsion system intended for a hydrogen-powered regional aircraft. The main innovation lies in the systematic treatment of all the electrical and thermal components to model the overall system performance. One of the main objectives is to study the feasibility of using the liquid hydrogen (LH_2) fuel to provide cryogenic cooling to the cryoelectric propulsion system and, thereby, enable ultracompact designs. Another aim has been to identify the optimal working point of the fuel cell to minimize the overall propulsion system's mass. The full mission profile is evaluated to make the analysis as realistic as possible. Analyses are done for three different 2035 scenarios, where available data from the literature are projected to a baseline, conservative, and optimistic scenario. The results show that the total propulsion system's power density can be as high as 1.63 kW/kg in the optimistic scenario and 0.79 kW/kg in the baseline scenario. In the optimistic scenario, there is also sufficient cryogenic cooling capacity in the hydrogen to secure proper conditions for all components, whereas the dc/dc converter falls outside the defined limit of 110 K in the baseline scenario.**

***Index Terms*— Cold power electronics (CPEs), cryoelectric propulsion, fuel cells, high-temperature superconductor (HTS) cables, hydrogen-powered aviation, proton-exchange membrane fuel cell (PEMFC), regional aircraft, superconducting machines, thermal modeling.**

NOMENCLATURE

A. Symbols

$A_{\mathrm{FC,eff}}$	Fuel cell total effective area [m^2].
a_{pol}, b_{pol}	Coefficients in linear approximation of polarization voltage [Vcm^2/A], [V].
$c_{p,\mathrm{air}}$	Specific heat capacity of air, 1.0 kJ/(kg · K).
F	Faraday's constant, 96 485 C/mol.
h	Specific enthalpy [J/kg] and altitude [m].
$\Delta h_{H_2,\mathrm{HHV}}$	Higher heating value of H_2, $1.418 \cdot 10^5$ kJ/kg.
j_{cell}	Fuel cell current density [A/cm^2].
k_1	Constant in expression for T_{amb}, 42 361 m.
m	Mass [kg].
$\dot{m}$	Mass flow [kg/s].
M_{air}	Molar mass of air, 28.9646431 g/mol.
Ma	Mach number [-].
n	Rotational speed [rpm].
p	Pressure [Pa].
p_0	Ambient pressure at MSL, 101 324 Pa.
pq_{TMS}	TMS power consumption per unit heat load removed [-].
P	Power [W].
PF	Power factor [-].
PTW	Power-to-weight ratio [kW/kg].
qm_{TMS}	Inverse specific weight of TMS [kJ/(s · kg)].
$\dot{Q}$	Heat load [J/s].
$R_{\mathrm{sp,air}}$	Specific gas constant of air, 0.28704 kJ/(kg · K).
T	Temperature [K].
T_0	Ambient temperature at MSL, 288.15 K.
t_{cruise}	Variable term in cruise mission duration [s].
TTW	Torque-to-weight ratio [Nm/kg].
ΔT_{ISA}	Temperature difference from ISA at MSL, 24 K.
U	Voltage [V].
x_{O_2}	Molar fraction of O_2 in air, 0.209.

B. Greek Letters

η	Efficiency [-].
$\eta_{\mathrm{comp,el}}$	Compressor motor efficiency, 0.94 [9].
$\eta_{\mathrm{comp},m}$	Mechanical compressor efficiency, 0.97 [9].
$\eta_{\mathrm{comp,pc}}$	Compressor converter efficiency, 0.95 [9].
$\eta_{\mathrm{comp},s}$	Isentropic compressor efficiency, 0.76 [9].
η_{pr}	Pressure recovery, 0.75 [9].
γ_{air}	Ratio of specific heats for air, 1.4.
λ	Used for ratios [-].
$\lambda_{H_2,\mathrm{net}}$, λ_{O_2}	Stoichiometric ratios for H_2 and O_2 [-].
ρ	Mass density [kg/m], [kg/m^2], [kg/kW], and [kg/(kg/s)].

C. Subscripts

amb	Ambient.
aux	Fuel cell auxiliary components.
avg	Average.
BoP	Balance of plant.

Manuscript received 30 November 2021; revised 8 March 2022; accepted 22 April 2022. Date of publication 29 April 2022; date of current version 21 October 2022. This work was supported in part by the Research Council of Norway (RCN) under Grant 259860 (Doctoral Scholarship). *(Corresponding author: Christian Hartmann.)*

Christian Hartmann is with the Institute for Energy Technology (IFE), 1777 Halden, Norway, and also with the Department of Electric Power Engineering, Norwegian University of Science and Technology (NTNU), 7034 Trondheim, Norway (e-mail: christian.hartmann@ife.no).

Jonas Kristiansen Nøland, Robert Nilssen, and Runar Mellerud are with the Department of Electric Power Engineering, Norwegian University of Science and Technology (NTNU), 7034 Trondheim, Norway (e-mail: jonas.k.noland@ntnu.no; robert.nilssen@ntnu.no; runar.mellerud@ntnu.no).

Digital Object Identifier 10.1109/TTE.2022.3170827

cell	Single fuel cell.
c	Cold.
comp	Compressor.
DCAC	DC/AC motor inverter.
DCDC	DC/DC converter.
eff	Effective.
el	Electrical.
exh	Exhaust.
FC	Fuel cell.
FCHX	Fuel cell heat exchanger.
HHV	Higher heating value.
HTS	High-temperature superconductor.
hum	Humidifier.
in	Inlet.
max	Maximum.
out	Outlet.
prop	Propeller.
SCM	Superconducting motor.
stack	Fuel cell stack.
stat	Static.
TMS	Thermal management system.
tot	Total.
w	Warm.

I. Introduction

HYDROGEN-POWERED aviation has received a renewed interest over the last few years due to its attractive promises of decarbonizing air transport [1]. There is also a push to utilize hydrogen as a sustainable fuel in other sectors as well, including hydrogen fuel cell vehicles (FCVs) [2], hydrogen trains (hyrail) [3], and hybrid fuels cells in marine vessels [4], to name a few.

In general, the energy density of the onboard energy storage is seen as the main limiting factor to scale up climate-neutral aviation for battery-electric architectures [5]. However, hydrogen is a much lighter energy source for aviation [1]. Hydrogen-powered aviation is also desired to be fully electric to not only deal with CO_2 emissions but also non-CO_2 emissions. A further step is to make the propulsion system cryoelectric, where the hydrogen fuel is stored as liquid hydrogen (LH_2) and used for both electric power generation and cooling of the electrical components. Due to the cryogenic temperature of the LH_2, the electrical machine and power transmission systems can be made superconducting, which is projected to dramatically reduce the size of the propulsion system [6], without the need to add weight-intensive cryocoolers. Another way to cut aircraft weight is to pursue multifunctional (MF) materials, integrating both mechanical and electrical properties [7].

In this study, we investigate a hydrogen-powered cryoelectric propulsion system where a proton-exchange membrane fuel cell (PEMFC) provides electrical energy to feed SCMs for propulsion. The hydrogen that goes into the PEMFC is also used for cryogenic cooling of the SCMs and high-temperature superconductor (HTS) cables and, furthermore, to provide cryogenic conditions for cold power electronics (CPEs). In this way, it is possible to minimize or fully eliminate the cryocoolers, which would otherwise be necessary to cool the components. Cryocoolers represent a significant mass and efficiency penalty to superconducting energy conversion systems [8].

Introducing airworthy aircrafts with a cryoelectric propulsion system represents a large challenge in several areas [1]. The involved technologies are currently immature and must be developed to become safe, reliable, and compact. Embedding hydrogen tanks into the airframes may require radical redesigns. A whole new fuel infrastructure must be established, and hydrogen production must be scaled up in order to become more competitive with traditional fuels. Furthermore, the licensing process will require revised and new standards.

Currently, the main efforts are directed toward finding technological solutions that will make it possible to scale up hydrogen-powered aircrafts. The technology is currently at a low technological readiness level (TRL), which makes cost assessments difficult. The exception is the hydrogen fuel itself, which is already an industrial commodity. It is presently too expensive to compete with conventional jet fuel, but the cost is projected to drop significantly in the decades to come [1].

One of the main scientific questions that we seek to answer in this study is whether there is an energy balance between the hydrogen consumption in the fuel cell and the heat loads in the cryogenic cooling loop at all operating points during a flight mission of a typical regional aircraft.

Numerous studies have been performed on the components that together constitute the full system [8]–[12], but these studies are either conducted on other system architectures or on single components that overlook the important system considerations. The concept of using hydrogen for cryogenic cooling has also been investigated in detailed studies, e.g., [13]. These studies provide important insights into the concepts and mechanisms of the system that we want to investigate, but they do not provide a sufficient basis for understanding the interdependencies between the components and the cooling system.

The main contribution of this article lies in the comprehensive framework where the component sizing and operation points of a cryogenic propulsion system for a next-generation hydrogen-powered aircraft are analyzed as a whole.

This article is organized with the following structure. First, the objective and the scope of the study are described in Section II. Next, Section III describes the mission profile considered and the ambient conditions. Then, the cryoelectric architecture is described in detail in Section IV, before the complete model framework is comprehensively described in Section V. The model implementation and analysis of the results from the simulated scenarios are presented in Section VI, before an outline of further research items is presented in Section VII.

II. Objectives, Scope, and Simplifications

The work presented herein investigates the cryoelectric architecture in Fig. 1. It is electrified by a hydrogen-fueled PEMFC, providing power downstream to an SCM. The power to the motor is transmitted via HTSs with CPE converters at each end. At the downstream end, the SCM drives a propeller,

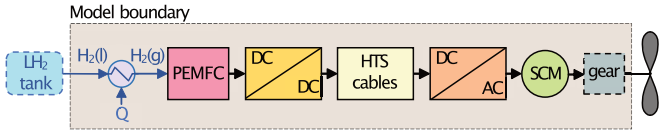

Fig. 1. Principal arrangement of the system investigated herein, where the PEMFC is the proton-exchange membrane fuel cell, the HTS cables are high-temperature superconductor, and the SCM is a superconducting machine.

TABLE I
TARGET VALUES FOR THE COMPLETE CRYOELECTRIC PROPULSION SYSTEM

Objective	Target
Utilize LH_2 fuel for cryocooling	$T_{SCM,max} < 25$ K (MgB_2) or $T_{SCM,max} < 60$ K (REBCO)
	$T_{HTS,max} < 77$ K
	$T_{DCAC,max} < 110$ K
	$T_{DCDC,max} < 110$ K
Power density	$PTW_{tot} > 1$ kW/kg

either directly or via a gearbox. Both configurations will be explored in this study. The hydrogen fuel is stored as a liquid (LH_2) at 20 K.

The main objectives of the study are given as follows.

1) Investigate if and to what extent the LH_2 fuel can also be utilized for cryogenic cooling of superconductors and CPEs at all modes of operation.
2) Analyze if the system in Fig. 1 can be realized with sufficient power density to enable the cryoelectric propulsion concept to be scalable.

In Table I, the main objectives are quantified in detail. The superconductors and converters dictate the maximum allowable hydrogen temperatures. The PTW target for the system inside the model boundary in Fig. 1, PTW_{tot}, is set in accordance with up-to-date aviation industry targets. This is ambitious because aerospace-grade fuel cells cannot be trusted to achieve more than 1 kW/kg at the present, which is currently the bottleneck of hydrogen–electric propulsion systems. However, technology experts believe that fuel cell power densities of 4 kW/kg could be possible by 2024 [14].

As of today, the technologies involved have not reached readiness levels where they can be considered for aircraft applications. It is, therefore, attempted to project results and trends reported in the literature to a 2035 scenario. To account for the difficulties and inevitable errors in predicting future performance data, we operate with three different 2035 scenarios, i.e., a conservative, an optimistic, and a baseline scenario, respectively. In general, the conservative and optimistic scenarios represent what are believed to be the worst and best interpretations of available data. The baseline values are set near the middle of the two extremes.

The boundary of the system model is shown in Fig. 1. The only energy source in the system is the LH_2, and the SCMs consume all net output power from the PEMFC. There are no energy buffers, so all required power is assumed to be instantly available from the PEMFC. Startup and transient behavior are not considered. Each point of operation through the flight mission is modeled as a steady state, and the timestep between each calculation point is 2.5 s. With the exception of the PEMFC, all components are modeled as having fixed efficiencies that do not vary over the operation points. Moreover, the system has no redundancy or protection systems.

TABLE II
AIRCRAFT DATA

PAX	Max. range	Max. total motor power	Max. propeller speed	MTOW
70	1200 km	4.1 MW ($2 \cdot 2.05$ MW)	1200 rpm	23 000 kg

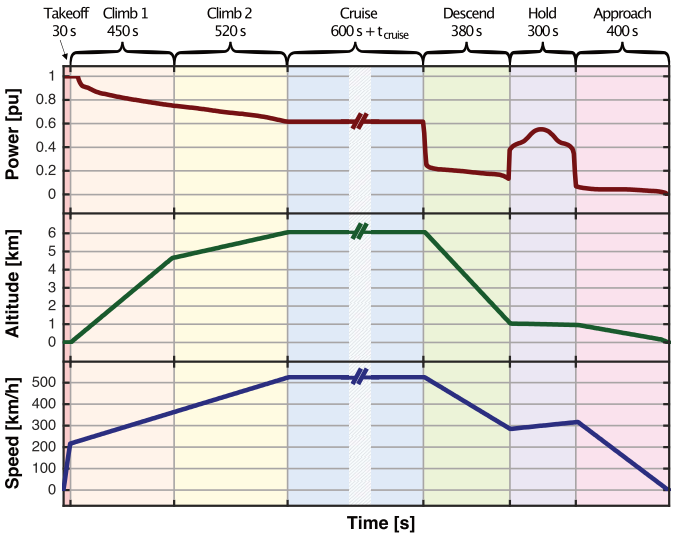

Fig. 2. Complete mission profile adopted from Jux *et al.* [15] for power, altitude, and speed. Base power is 4.1 MW p.u. The cruise phase has been truncated in this study since the time-dependent variables are static during this phase. The actual duration will be 600 s + t_{cruise}.

The system is rated for a total power of 4.1 MW, suitable for a twin-engine single-aisle 70-seater aircraft [15]. The aircraft data is very similar to that of an ATR 72-600 (see Table II).

III. MISSION PROFILE AND ATMOSPHERIC CONDITIONS

The mission profile and atmospheric conditions have a significant impact on the rating of the components. A detailed mission profile for the hybrid–electric regional aircraft in Table II has been developed by Jux *et al.* [15]. It is adopted in this work due to its relevant and detailed power profile. The altitude and speed profiles have been simplified by dividing the mission phases into piecewise linear segments. The resulting mission profile is shown in Fig. 2. The cruise phase has been truncated since the conditions remain static during this phase, and the total hydrogen consumption is not the focus of this study.

The model framework developed for this study is not reliant on this specific mission profile. It can be used to analyze other applications with significantly different mission profiles, power levels, and so on.

The International Standard Atmosphere (ISA) defines ambient pressure and temperature expressions as a function of

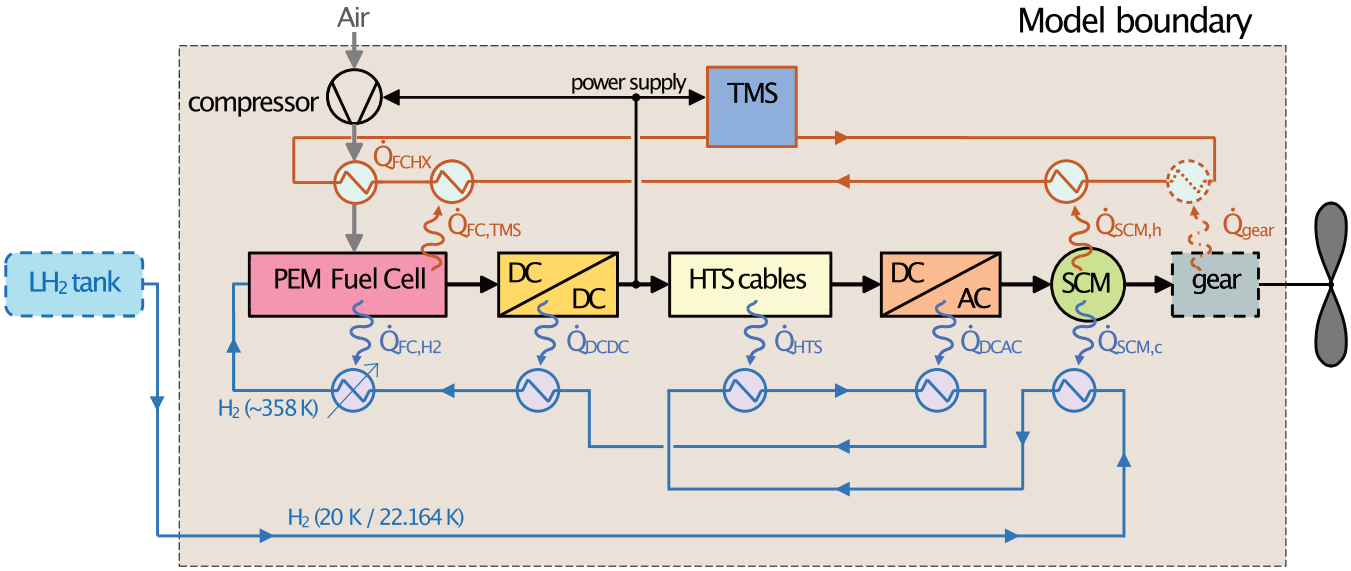

Fig. 3. More detailed representation of Fig. 1, including the model of the cooling arrangements, the TMS, and the fuel cell compressor.

elevation above mean sea level (MSL), as mathematically described in (1) and (2). These will be used to determine the atmospheric conditions over the mission profile in Fig. 2 to be used in the fuel cell modeling in Section V-H. The ISA models [16] assume an ambient temperature $T_0 = 288.15$ K (15 °C) at MSL. As this temperature is not representative of hot-day conditions, it is necessary to include a corrective term. The last term in (2) has been added to yield results consistent with the "hot" nonstandard atmosphere defined in MIL-STD-210A [17], [18] in the altitude range of 0–6500 m. Finally, ΔT_{ISA} is set to 24 K, which yields a temperature of 39 °C at MSL

$$p_{\mathrm{amb}} = p_0\left(1 - 0.0065 \cdot \frac{h}{T_0}\right)^{5.2561} \tag{1}$$

$$T_{\mathrm{amb}} = T_0 - 6.5\frac{h}{1000} + \Delta T_{\mathrm{ISA}}\left(1 - \frac{h}{k_1}\right). \tag{2}$$

IV. Cryoelectric Propulsion System

This section describes the key components in the considered cryoelectric propulsion system, including TMSs, cryogenic cooling loops, and heat exchange dynamics with hydrogen.

A. Breakdown of All Energy Flows

Fig. 3 shows the system model with cooling circuits, TMS, and a fuel cell compressor included. The blue cooling circuit shows how the hydrogen fuel is directed to provide cryogenic cooling of the SCM, HTS cables, and the power electronics before it enters the fuel cell.

Since hydrogen fuel does not have sufficient heat capacity to take out all the losses in the system, an additional conventional cooling circuit is required. This is the TMS circuit, drawn with arrows in orange in Fig. 3. It is mainly the heat loads from the PEMFC that go into the TMS but noncryogenic heat loads from the SCM and gear (when included) also contribute. The TMS consumes electrical power to do this work.

A compressor is required to compress the ambient air before it is fed into the PEMFC's cathode. The airflow is drawn in gray in Fig. 3. Since the temperature of the air increases as it is compressed, it is also necessary to have a heat exchanger (HX) where the excess heat built up over the compressor can be removed in order to maintain optimum air temperature at the cathode inlet.

It can be seen from Fig. 3 that the dc/dc converter must be dimensioned to supply power to the compressor and the TMS in addition to the power delivered to the SCM.

In this study, the hydrogen supplied from the tank is modeled as being either fully liquid at 20 K or saturated vapor at 22.164 K.

B. Cryogenic Cooling Loop

One of the main objectives of this study is to investigate the feasibility of using the LH_2 fuel to provide cryogenic cooling of superconductors and power electronic components. There is a very valuable synergy if this can be achieved. First, it enables the use of highly compact and efficient SCMs, HTS transmission, and CPE. Second, the cryocoolers that otherwise would be required to cool the superconductors can be eliminated or minimized, which means large savings in weight and power consumption. Third, it becomes unnecessary to have an extra HX between the LH_2 tank and the PEMFC.

It is imperative that the cryogenic temperatures stay strictly within limits dictated by the types of superconductors used in the SCM and the HTS cables. For the SCM, this temperature limit is set either to 25 K or 60 K, depending on whether MgB_2 or REBCO is used. It is assumed that REBCO is used for the HTS cables, and they can be operated at temperatures up to 77 K since the loss generated over a superconducting dc transmission is small.

It has also been reported that power electronic components can be made much more compact and efficient if they are allowed to operate at cryogenic temperatures. The operational

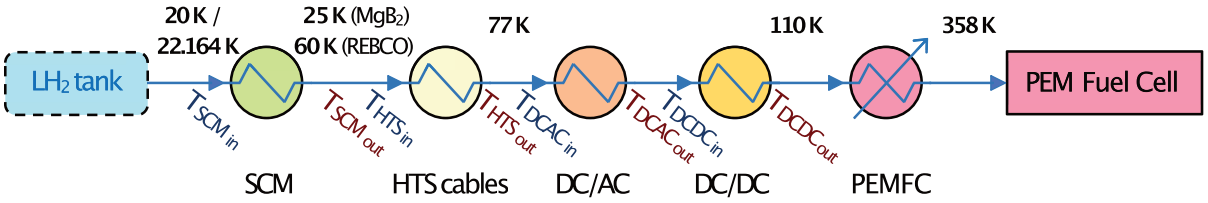

Fig. 4. Sequence of components arranged according to the flow of cryogenic coolant from the LH_2 tank to the PEM fuel cell.

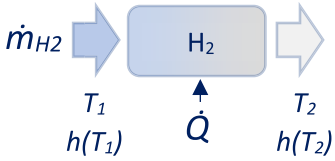

Fig. 5. Hydrogen mass flow through a control volume with heat input $\dot{Q}$ to the medium between two temperature levels (T_1 and T_2).

temperature limit for CPE does not seem to be exactly defined. Here, 110 K will be used as an indicative value [13], but, unlike superconductors, there is no abrupt and detrimental transition if this temperature is exceeded.

After the heat from the superconductors and power electronics has been absorbed by the hydrogen, the remaining heat required to bring the hydrogen to 85 °C (inlet temperature at the PEMFC) is absorbed from the heat loss in the PEMFC. As mentioned previously, this heat only constitutes a small fraction of the total heat produced in the PEMFC. The remaining heat loss needs to be removed by the TMS, as illustrated in Fig. 3.

The cryogenic cooling loop from Fig. 3 is redrawn in Fig. 4 with the components arranged in the sequence in which they exchange heat with the hydrogen. The temperature limits are also defined in the figure.

C. Heat Exchange With Hydrogen

Hydrogen has a high heat capacity, which makes it an excellent cryogenic coolant. The specific heat capacity is about 12 kJ/(kg·K), but this value varies over the temperature range being studied. For this reason, it is convenient to use the specific enthalpy of hydrogen to determine the temperature increase as a function of loss-heat absorbed by the hydrogen. Enthalpy tables are provided on the website of the National Institute of Standards and Technology (NIST) [19].

The hydrogen-cooled components are modeled as control volumes. When subjected to a constant hydrogen mass flow $\dot{m}_{H2}$ and heat influx $\dot{Q}$, the temperature rise is related to the change in enthalpy over the components [see Fig. 5, and (3) and (4)]. It is assumed that the only heat $\dot{Q}$ transferred to the hydrogen originates from the heat losses generated in the components

$$h(T_2) = h(T_1) + \frac{\dot{Q}}{\dot{m}_{\mathrm{H_2}}} \tag{3}$$

$$T_2 = T(h_2). \tag{4}$$

The hydrogen pressure is set equal to the PEMFC anode pressure (1.66 bar). For simplicity, the pressure drop over the components is neglected.

In the models, the hydrogen can be either gaseous (GH_2) or liquid (LH_2) when it is fed into the cryogenic cooling circuit. In the cases where it is modeled as being liquid, it is necessary to take the hydrogen's latent heat of vaporization into account. During the phase change at 22.164 K, the hydrogen absorbs 438 kJ/kg before it is fully vaporized. Such two-phase cooling significantly increases the cooling capacity of the cryogenic cooling loop compared to purely gaseous cooling.

V. Model Framework for Component Sizing

The framework for power and heat load balance, as well as component sizing, is further developed in this section.

A. Component-Level Loss Modeling

The sizing of the components is done in the upstream direction, starting with the gearbox. This is done to correctly account for the efficiency of the various components since each consecutive component must have a power rating sufficient to supply not only useful power but also the downstream losses.

Iteration is required to determine the power balance of the PEMFC and the compressor/TMS due to the components' interdependency. The description of how this balancing is done is deferred to Section VI-A when the simulation model is described.

The input power to a component is given by

$$P_{\mathrm{in}} = P_{\mathrm{downstr}} + \dot{Q}_{\mathrm{loss}} \tag{5}$$

where

$$\dot{Q}_{\mathrm{loss}} = P_{\mathrm{downstr}}\left(\frac{1}{\eta} - 1\right) \tag{6}$$

where P_{downstr} is the sum of useful power and accumulated losses of all components downstream. $\dot{Q}$ and η are the loss and efficiency of the component being sized.

B. Gearbox Sizing

Connecting a gearbox between the SCM shaft and the propeller allows for choosing an SCM shaft speed different from the propeller speed. The benefit of this is that the mass and volume of the SCM can be reduced when it is designed for higher rotational speeds. However, some of this reduction will be offset by the mass and volume of the gearbox. Gearboxes also introduce an increased loss in the system.

Equation (7) is based on data from reference [20]. It estimates the gearbox mass as a function of the transmitted power and the speed (in rpm) of the SCM rotor and the propeller

$$m_{\mathrm{gear}} = k_{\mathrm{gear}} \frac{(P_{\mathrm{SMC}})^{0.76} \cdot (n_{\mathrm{SMC}})^{0.13}}{(n_{\mathrm{prop}})^{0.89}}. \tag{7}$$

TABLE III
SIMULATION PARAMETERS, GEARBOX

Parameter	Symbol	2035 scenario		
		Conservative	Baseline	Optimistic
Sizing factor [-]	k_{gear}	0.25	0.21	0.17
Efficiency [%]	η_{gear}	98.5	99.0	99.5

TABLE IV
RECENT SCM REFERENCE STUDIES

	Study	
	Boll et al. [10]	Filipenko et al. [12]
SCM type	Fully SC	Partially SC (SC rotor)
Power [MW]	10.5	10.0
Speed [rpm]	3500	7000
El. frequency [Hz]	350	467
Power factor [-]	-	0.89
Heat load to cryogen [kJ/s]	2.40	0.07
Heat load to TMS [kJ/s]	5.68	200
Efficiency [%]	99.92	98.00
Weight [kg]	303	500
PTW [kW/kg]	34.7	20
TTW [Nm/kg]	94.5	27.3

A value of $k_{\text{gear}} = 0.21$ gives results consistent with reference [20]. This is set as the baseline value. 20% mass is added and subtracted for the conservative and optimistic estimates, respectively.

The efficiency of the gearbox is dependent on the operating point. Boll *et al.* [10] report efficiencies reaching 99.6%, whereas other studies report lower efficiencies, in the range 96%–99% [8], [21].

Table III summarizes the gearbox parameters considered in this study.

C. Superconducting Motor Sizing

Table IV summarizes the main results from two recent design studies performed on SCMs for aircraft applications. The first machine [10] is a fully superconducting propulsion motor. The second machine [12] is a generator with superconducting distributed field coils in the rotor and conventional copper armature windings on the stator.

Both studies report a significant loss increase with increasing frequency. Therefore, the maximum speed is limited to either 1200 (direct drive) or 3500 rpm (geared drive) in the model simulations. Since the maximum speed is varied, the TTW ratio is used to size the machines. The PTW ratio can be found from the following equation:

$$\text{PTW}_{\text{SMC}} = \frac{\pi}{30} n_{\text{SMC}} \text{TTW}_{\text{SMC}} \cdot 10^{-3}. \tag{8}$$

The three simulation scenarios for the SCM are set with quite a wide span between the conservative and the optimistic scenario. This is to account for the possibility of using different SCM topologies (fully superconducting, partially superconducting, yokeless, and so on). The SCM parameters will also be investigated individually in a sensitivity study to gain an understanding of how the SCM parameters impact the total system.

TABLE V
SIMULATION PARAMETERS, SCM

Parameter	Symbol	2035 scenario		
		Conservative	Baseline	Optimistic
TTW [Nm/kg]	TTW_{SCM}	30	60	90
"Cold" efficiency [%]	$\eta_{SCM,c}$	99.0	99.5	99.9
"Warm" efficiency [%]	$\eta_{SCM,w}$	98.0	99.0	99.5
Power factor [-]	PF_{SCM}	0.80	0.89	0.92
Speed [rpm]	n_{SCM}	1200/3500	1200/3500	1200/3500

TABLE VI
SIMULATION PARAMETERS, DC/AC MOTOR INVERTER

Parameter	Symbol	2035 scenario		
		Conservative	Baseline	Optimistic
PTW [kW/kg]	PTW_{DCAC}	20	25	35
Efficiency [%]	η_{DCAC}	99.0	99.3	99.8

In Table V, the motor efficiency is split into a "cold" and a "warm" contribution. This is done to separate the losses discharged to the cryogenic cooling loop and the TMS cooling loop. The total efficiency of the motor is given by

$$\eta_{\text{SMC,tot}} = \frac{1}{\frac{1}{\eta_{\text{SMC},c}} + \frac{1}{\eta_{\text{SCM},w}} - 1}. \tag{9}$$

D. DC/AC Motor Inverter Sizing

Various performance metrics for CPE motor inverters have been reported. The PTW ratios span from 19 [10] to 30 kW/kg [11], whereas the efficiencies are in the range 99.3% [22] to 99.98% [10].

Boeing has set target values of 99.3% efficiency and a PTW ratio of 26 kW/kg for the development of a three-level active neutral-point-clamped (ANPC) 1-MW cryogenic motor inverter operating at 1000-V input voltage [23]. The baseline scenario is set close to these values. Table VI lists the simulation parameters used for the DC/AC inverter.

The apparent power of the SCM must be accounted for in determining the inverter mass and loss, yielding

$$m_{\text{DCAC}} = \frac{P_{\text{in,SCM}}}{\text{PF}_{\text{SCM}} \text{PTW}_{\text{DCAC}}} \tag{10}$$

$$\dot{Q}_{\text{DCAC}} = \frac{P_{\text{in,SCM}}}{\text{PF}_{\text{SCM}}} \left(\frac{1}{\eta_{\text{DCAC}}} - 1 \right). \tag{11}$$

It follows from this that the efficiency seen from the input will be lower than η_{DCAC}. The input must supply the extra losses originating from the reactive currents. The *de facto* efficiency is reduced as a consequence of this. The efficiency seen from the input becomes

$$\eta'_{\text{DCAC}} = \frac{\text{PF}_{\text{SCM}}}{\frac{1}{\eta_{\text{DCAC}}} - 1 + \text{PF}_{\text{SCM}}}. \tag{12}$$

E. HTS Cable Sizing

The specific weight of dc HTS cables reported in the literature lies in the range of 5–14 kg/m [10], [24]–[26]. The power levels in these studies are higher than what is considered here. The HTS cryostat needs to be well-insulated

TABLE VII
SIMULATION PARAMETERS, HTS CABLES

Parameter	Symbol	2035 scenario		
		Conservative	Baseline	Optimistic
HTS specific mass [kg/m]	ρ_{HTS}	10	5	3
HTS total mass [kg]	m_{HTS}	270	135	81
Efficiency [%]	η_{HTS}	99.9	99.95	99.99

to minimize heat leaks. This requirement is relatively independent of the power transfer. However, the voltage and current loading have an impact on the mass of the HTS conduit since both these parameters dictate pole-to-pole and pole-to-ground distances [10]. In light of this, 5 kg/m seems like a reasonable baseline value for the specific weight of each HTS conduit.

The reference aircraft (ATR 72-600) has a length of 27 m and a wingspan of 27 m. The distance between the dc/dc converter and the motor inverter is roughly estimated to be one-quarter of the aircraft length and one-quarter of the wingspan. Hence, the required HTS cabling for each motor is 13.5 m such that the total HTS cable length is 27 m. This is a very coarse but conservative length estimate. The simulation parameters used for the HTS cables are summarized in Table VII.

F. Thermal Management System Sizing

Heat losses that are not absorbed by the hydrogen fuel must be removed by the TMS.

Although electric components are characterized by high efficiencies, they also have some inherent drawbacks when it comes to thermal management. The maximum admissible operating temperatures for most electrical components are low. This makes heat transfer and heat rejection costly since the mass and volume of key TMS components, such as HXs and cold plates, need to be large to compensate for the low-temperature differentials.

Electrical components must also be protected from particles and moisture. This reduces the ability to exchange heat with the surroundings.

The fact that the components' heat loads are at their highest at the beginning of take-off poses a special challenge [18], [27]. At this mission point, the ambient temperature is high, whereas the velocity of the surrounding air relative to the aircraft is low. Without a means to increase the velocity of the air passing through the HX, the TMS can become excessively bulky. A ram air-based TMS has been investigated in several studies [18], [22], [27], [28]. In this arrangement, the air is channeled through an HX, and its velocity is maintained by a ram fan. The principal arrangement is outlined in Fig. 6.

TMS performance data have been collected from five studies. The results are summarized in Table VIII.

The key metrics in Table VIII are listed in columns 5 and 6, where $\dot{Q}_{\text{TMS,max}}/m_{\text{TMS}}$ specifies the maximum heat loss that can be removed per kilogram of the TMS system. Moreover, $P_{\text{TMS,max}}/\dot{Q}_{\text{TMS,max}}$ specifies the TMS's power consumption per kJ/s of removed heat load.

In general, there is a relatively large spread in the performance values given in Table VIII. The authors of these studies have optimized the component masses and power

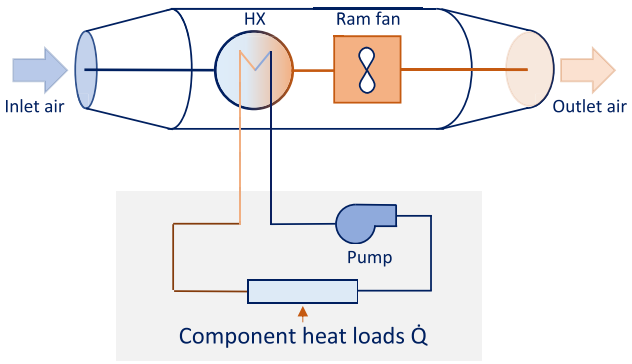

Fig. 6. Ram air-based TMS.

TABLE VIII
TMS PERFORMANCE DATA FROM FIVE AVAILABLE STUDIES

Study	m_{TMS} [kg]	$P_{TMS,max}$ [kW]	$\dot{Q}_{TMS,max}$ [kJ/s]	$\frac{\dot{Q}_{TMS,max}}{m_{TMS}}$ [kJ/(s·kg)]	$\frac{P_{TMS,max}}{\dot{Q}_{TMS,max}}$ [-]
Chapman et al. [29]	176	272	505	2.86	0.54
Rheaume and Lents [27]	250	30	209	0.83	0.14
Rheaume et al. [18]	78	17	210	2.70	0.08
Lents et al. [30]	152	51	221	1.45	0.23
Jansen et al. [22]	122.6	-	83	0.68	-

TABLE IX
SIMULATION PARAMETERS, TMS

Parameter	Symbol	2035 scenario		
		Conservative	Baseline	Optimistic
$\dot{Q}_{TMS,max}/m_{TMS}$ [kJ/(s·kg)]	qm_{TMS}	1.0	3.0	5.0
$P_{TMS,max}/\dot{Q}_{TMS,max}$ [-]	pq_{TMS}	0.15	0.08	0.04

consumption by carefully analyzing the transient conditions between mission points. The general principle is that the TMS is not dimensioned to sustain steady-state operation at peak power. As long as the components' maximum admissible temperatures are not exceeded during the relatively short duration of take-off and initial climbing, excess heat is allowed to be rejected at higher altitudes when the air velocity is high, and the ambient temperature is low. It is assumed that a similar optimization can be done for the system modeled here.

It is worth noting that the systems in Table VIII are designed for battery systems. Due to the low operating temperatures of batteries (<35–40 °C), the TMSs in Table VIII are expected to be heavier and consume more power per unit (p.u.) rejected heat load than will be the case with a PEMFC operating at a stack temperature of 85 °C.

For the optimistic 2035 scenario, it is speculated that further mass and power reduction can be achieved by also utilizing the aircraft's surface as a heat sink [31]. Table IX summarizes the parameter choices made for the three different scenarios.

G. Fuel Cell DC/DC Converter Sizing

A dc/dc converter is needed to match the fuel cell's low and variable output voltage with that of the dc distribution. Ideally, the dc/dc converter should be isolated from the fuel cell's output both for safety reasons and to avoid common-mode noise that reduces the lifetime of the fuel stack insulation layers [32]. However, to achieve sufficiently high power densities,

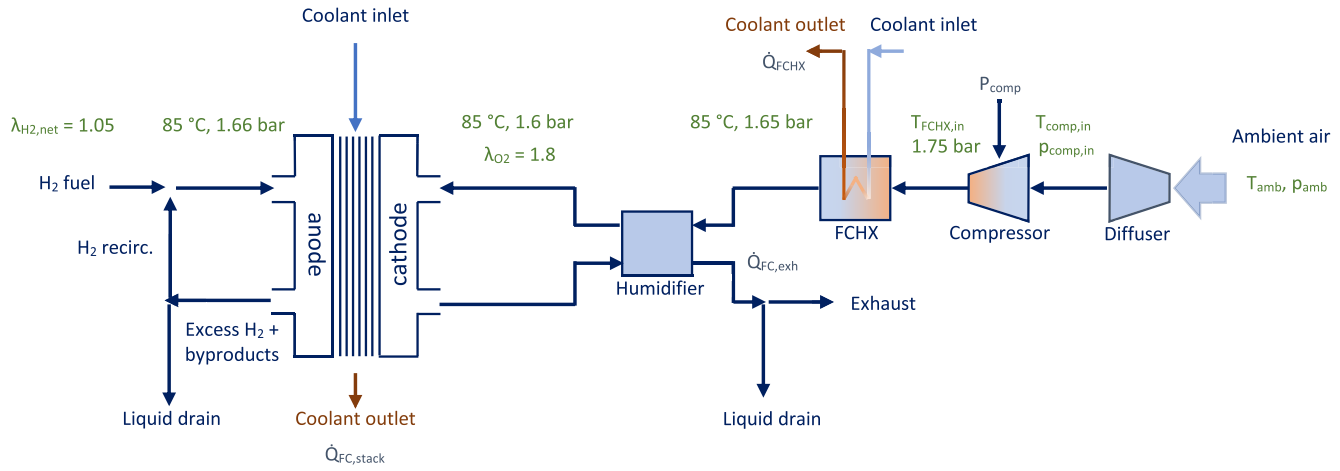

Fig. 7. Fuel cell and auxiliary components. Operating parameters (in green) are adopted from Schröder *et al.* [9].

TABLE X
SIMULATION PARAMETERS, DC/DC FUEL CELL CONVERTER

Parameter	Symbol	2035 scenario		
		Conservative	Baseline	Optimistic
PTW ratio [kW/kg]	PTW_{DCDC}	10	16	23
Efficiency [%]	η_{DCDC}	98.0	98.5	99.0

it seems to be necessary to develop a nonisolated topology for multimegawatt aircraft applications. The multilevel flying capacitor and multilevel buck/boost topologies are reported to be two alternatives of particular interest [33].

The authors have not been able to find published performance metrics on dc/dc converters operating at cryogenic temperatures. Warncke *et al.* [34] have published results on a conventionally cooled dc/dc converter for aircraft applications. They have achieved a power density of 8.3 kW/kg for the power module alone, which is similar to what can be achieved for an optimized motor inverter with current conventional technology [35]. By operating the dc/dc converter at cryogenic temperatures, it is anticipated that power density and efficiency are improved in a fashion similar to the motor dc/ac inverter. However, it is still necessary to account for filters and so on, which add weight to the dc/dc converter. It is, therefore, stipulated that the cryogenic dc/dc converter will have a specific weight 50% higher than the cryogenic motor inverter. The efficiencies for the dc/dc converter are also set more conservatively than for the motor inverter. Table X summarizes these notional values.

H. PEM Fuel Cell Sizing

Fig. 7 depicts the considered PEMFC model. In addition to the compressor and HX (FCHX) already described, the system comprises an air inlet diffuser, a humidifier, and balance-of-plant (BoP) components. The operating parameters, shown in green, are adopted from reference [9].

1) Required Fuel Cell Area: The electrical power output from a fuel cell is determined by the average cell voltage and the cell current density multiplied with the total active cell area in the fuel cell, yielding

$$P_{\mathrm{FC,el}} = U_{\mathrm{cell,avg}} j_{\mathrm{cell}} A_{\mathrm{FC,eff}}. \tag{13}$$

By rearranging (13), the required total effective cell area can be determined from

$$A_{\mathrm{FC,eff}} = \frac{P_{\mathrm{FC,el}}}{U_{\mathrm{cell,avg}} j_{\mathrm{cell}}}. \tag{14}$$

Here, $A_{\mathrm{FC,eff}}$ must be dimensioned for the highest output power during the mission.

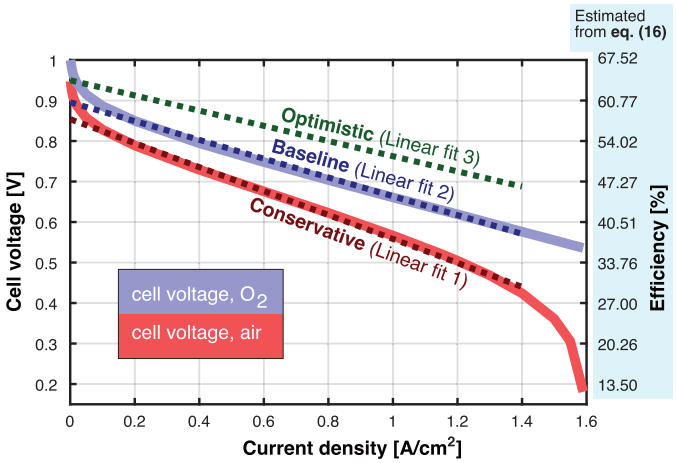

Fig. 8. Fuel cell polarization curves for air and oxygen, adopted from Barbir [36]. *Linear Fits 1–3* represent the approximations used in the conservative, baseline, and optimistic scenarios, respectively. Equation (16) is used to estimate the FC's efficiency for the y-axis on the right-hand side.

2) Fuel Cell Polarization Curves: The cell voltage is dependent on the current density in the fuel cell. This can be seen in the polarization plots in Fig. 8, extracted from Barbir [36].

The fuel cell's cathode can be fed with either air (air-breathing) or high-purity oxygen (air-independent) [37]. Fig. 8 shows how the cell voltage benefits from an air-independent operation.

In this study, only air-breathing configurations will be considered. For the conservative 2035 scenario, it is simply assumed that no improvements in the cell polarization curve

TABLE XI
COEFFICIENTS FOR APPROXIMATION OF POLARIZATION VOLTAGE

Linear approximation	a_{pol} [Vcm^2/A]	b_{pol} [V]
Linear Fit 1 (conservative)	-0.2957	0.8539
Linear Fit 2 (baseline)	-0.2320	0.8956
Linear Fit 3 (optimistic)	-0.1875	0.9500

compared to Fig. 8 have been accomplished. The *Linear Fit 1* curve is therefore employed in the conservative scenario.

Jiao *et al.* [38] have published a technology perspective for the performance of PEM fuel cells for automotive applications toward 2040. It is predicted that the PEMFC will operate at much higher current densities (4 A/cm^2) and higher cell voltages (0.8–0.9 V). These values represent a remarkable improvement in maximum cell power density (5.3 W/cm^2) compared to what is achievable with the polarization curve for an air-breathing PEMFC shown in Fig. 8 (0.6 W/cm^2).

Based on these promising projections, the polarization curve for the optimistic 2035 scenario is approximated by *Linear Fit 3* in Fig. 8. This is a very notional estimate. With this model, the maximum cell power density is still below 1 W/cm^2.

The baseline polarization curve is set to coincide with the air-independent curve in Fig. 8, which lies about halfway between the two extremes.

As can be seen from Fig. 8, the linear approximations closely match the actual polarization curves in the range 0.1 A $\leq j_{\text{cell}} \leq$ 1.4 A/cm^2. In practice, j_{cell} will never exceed 1.4 A/cm^2, but an error is introduced for current densities below 0.1 A/cm^2. This is deemed acceptable since this mode of operation only occurs for a very small part of the mission. Furthermore, it has no impact on the sizing of the components.

Table XI lists the coefficients a_{pol} and b_{pol} used for the three linear approximation curves *Linear Fits 1–3* to be used in (15).

The appropriate set of coefficients in Table XI can now be used to establish an approximate average cell voltage, yielding

$$U_{\text{cell,avg}} \approx a_{\text{pol}} \cdot j_{\text{cell}} + b_{\text{pol}}. \tag{15}$$

3) Fuel Cell Efficiency: The fuel cell efficiency is derived from the average cell voltage. Throughout this study, the HHV of hydrogen is used. When small parasitic phenomena are ignored, the fuel cell efficiency simply becomes [36]

$$\eta_{\text{FC,el,HHV}} = \frac{U_{\text{cell,avg}}}{1.481}. \tag{16}$$

4) Stoichiometric Ratios: The mass flow of hydrogen fed into the anode is always larger than the mass flow that goes into the fuel cell reaction. The ratio between these mass flows is given by the stoichiometric ratio, which is always greater than one. This means that the anode output will contain unutilized hydrogen. This hydrogen can be rejected as exhaust, but this leads to poor fuel efficiency. The alternative is either to recycle the excess hydrogen from the anode output by feeding it back into the main fuel line or to employ dead-end anode operation [39]. The former approach is assumed here, as shown in Fig. 7.

The stoichiometric ratio λ_{O_2} on the cathode side is also greater than one. The stoichometric ratios used in this article are adopted from Schröder *et al.* [9]. There, a net stoichiometric ratio of $\lambda_{\text{H}_2,\text{net}} = 1.05$ is achieved through hydrogen recirculation. Also, $\lambda_{\text{O}_2} = 1.8$ is assumed.

5) Mass Flow: The required mass flow of hydrogen is now given by

$$\dot{m}_{\text{H}_2,\text{in}} = \frac{\lambda_{\text{H}_2,\text{net}} P_{\text{FC,el}}}{\eta_{\text{cell}} \Delta h_{\text{H}_2,\text{HHV}}}. \tag{17}$$

On the cathode side, the air mass flow is given by [37]

$$\dot{m}_{\text{air,in}} = \frac{j_{\text{cell}} A_{\text{FC,eff}}}{4F \cdot x_{\text{O}_2}} \lambda_{\text{O}_2} M_{\text{air}}. \tag{18}$$

6) Chemical Power Delivered to the PEMFC: The chemical power (HHV) delivered to the fuel cell is calculated

$$P_{\text{H}_2,\text{HHV}} = \dot{m}_{\text{H}_2,\text{in}} \Delta h_{\text{H}_2,\text{HHV}}. \tag{19}$$

7) Compressor Power: The ambient temperature and pressure are given by (1) and (2). The required cathode compressor power (P_{comp}) can now be established by first calculating the specific enthalpy change over the compressor, then scaling for cathode air mass flow, and adjusting for compressor efficiencies. Equations (20)–(24) have been adopted from Schröder *et al.* [1], Struchtrup [40], and Lombardi *et al.* [41]. For simplicity, the input filter has been omitted from the model.

The compressor inlet temperature can be formulated

$$T_{\text{comp,in}} = T_{\text{amb}} + \frac{(\sqrt{\gamma_{\text{air}} R_{\text{sp,air}} T_{\text{amb}}} \cdot Ma)^2}{2c_{p,\text{air}}}. \tag{20}$$

The maximum achievable static pressure at the compressor inlet is given by

$$p_{\text{comp,in,stat}} = p_{\text{amb}} \left(\frac{T_{\text{comp,in}}}{T_{\text{amb}}} \right)^{\frac{\gamma_{\text{air}}}{\gamma_{\text{air}}-1}}. \tag{21}$$

The pressure at the compressor inlet is found from

$$p_{\text{comp,in}} = \eta_{\text{pr}} (p_{\text{comp,in,stat}} - p_{\text{amb}}) + p_{\text{amb}}. \tag{22}$$

Change in specific enthalpy is expressed as

$$\Delta h_{\text{comp}} = \frac{1}{\eta_{\text{comp},s}} c_{p,\text{air}} T_{\text{comp,in}} \left[\left(\frac{p_{\text{FCHX,in}}}{p_{\text{comp,in}}} \right)^{\frac{R_{\text{sp,air}}}{c_{p,\text{air}}}} - 1 \right]. \tag{23}$$

Finally, the required compressor power is

$$P_{\text{comp}} = \frac{\Delta h_{\text{comp}} \dot{m}_{\text{air,in}}}{\eta_{\text{comp},m} \eta_{\text{comp,el}} \eta_{\text{comp,pc}}}. \tag{24}$$

8) Heat Rejected to FCHX: The temperature at the compressor's outlet can be approximated by

$$T_{\text{FCHX,in}} \approx T_{\text{comp,in}} + \Delta h_{\text{comp}}. \tag{25}$$

Setting $\Delta T_{\text{comp}} \approx \Delta h$ (in kJ/kg) is a good approximation in the 200 K–550 K temperature range.

The heat rejected from the fuel cell's HX is estimated as

$$\dot{Q}_{\text{FCHX}} = c_{p,\text{air}} \dot{m}_{\text{air,in}} (T_{\text{FCHX,in}} - T_{\text{FCHX,out}}). \tag{26}$$

9) Heat Rejected From the Fuel Cell Stack: The HHV chemical power that contributes to the reaction in the fuel cell is given by

$$P_{\mathrm{H_2,HHV,eff}} = P_{\mathrm{H_2,HHV}} \frac{1}{\lambda_{\mathrm{H_2,net}}}. \tag{27}$$

The total thermal loss in the PMFC is found from

$$\dot{Q}_{\mathrm{FC,stack}} + \dot{Q}_{\mathrm{FC,exh}} = P_{\mathrm{H_2,HHV,eff}} - P_{\mathrm{FC,el}}. \tag{28}$$

Here, the thermal loss has been split into two terms. The first term, $\dot{Q}_{\mathrm{FC,stack}}$, represents the heat load that must be removed from the stack by the TMS. The second term, $\dot{Q}_{\mathrm{FC,exh}}$, represents the heat load rejected at the cathode exhaust. The fraction of the total thermal losses rejected to the TMS is approximated by $\lambda_{\mathrm{FC,TMS}}$. This fraction is coarsely estimated to be 0.95 [42]. Each of the terms on the left-hand side of (28) can, thus, be written as

$$\dot{Q}_{\mathrm{FC,stack}} = \lambda_{\mathrm{FC,TMS}}(P_{\mathrm{H_2,HHV,eff}} - P_{\mathrm{FC,el}}) \tag{29}$$

$$\dot{Q}_{\mathrm{FC,exh}} = (1 - \lambda_{\mathrm{FC,TMS}})(P_{\mathrm{H_2,HHV,eff}} - P_{\mathrm{FC,el}}). \tag{30}$$

10) Mass Estimates: The PEMFC mass estimate is based on the weight of the fuel cell stack, the compressor, and the humidifier. This is in accordance with the approach of Schröder *et al.* [9]. In addition, a mass overhead is added to account for the remaining balance of plant (BoP) components, structural materials, and so on.

The fuel cell mass is calculated from the total effective cell area, yielding

$$m_{\mathrm{stack}} = \rho_{A,\mathrm{FC,eff}} \cdot A_{\mathrm{FC,eff}}. \tag{31}$$

Correspondingly, the masses of the compressor and humidifier are calculated from the power densities of the respective components, yielding

$$m_{\mathrm{comp}} = \rho_{\mathrm{comp}} \cdot P_{\mathrm{comp}} \tag{32}$$

$$m_{\mathrm{hum}} = \rho_{\mathrm{hum}} \cdot \dot{m}_{\mathrm{air,in}}. \tag{33}$$

Finally, the overhead mass for BoP and so on is taken as a fraction of the sum of the masses from (31) to (33), yielding

$$m_{\mathrm{BoP}} = \lambda_{\mathrm{BoP}}(m_{\mathrm{stack}} + m_{\mathrm{comp}} + m_{\mathrm{hum}}). \tag{34}$$

11) Choice of Parameters for PEMFC Simulation Scenarios: The simulation parameters for the PEMFC are given in Table XII.

The mass parameters for the conservative scenario have been set in accordance with Schröder *et al.* [9]. The exception is the BoP overhead factor (last row), which has been set subjectively.

The optimistic compressor mass density estimate is set to 0.3 kg/kW. It is here assumed that a superconducting machine is employed to drive the compressor. This will necessitate hydrogen cooling, which would lead to a small increase in hydrogen temperatures. This is neglected here due to the low power rating of the compressor motor relative to the propulsion motors. It is also assumed that the humidifier mass density can be reduced moderately, while the BoP overhead factors are kept unchanged.

TABLE XII
SIMULATION PARAMETERS, PEMFC

Parameter	Symbol	2035 scenario		
		Conservative	Baseline	Optimistic
Polarization curve coeffs. [-]	a_{pol}, b_{pol}	Lin. fit 1	Lin. fit 2	Lin. fit 3
Fuel stack mass density [kg/m^2]	$\rho_{A,FC,eff}$	2.5	1.65	0.8
Compressor mass density [kg/kW]	ρ_{comp}	0.53	0.4	0.3
Humidifier mass density [kg/(kg/s)]	ρ_{hum}	82.35	70	60
Fuel cell BoP overhead factor [-]	λ_{BoP}	0.2	0.2	0.2

Jiao *et al.* [38] predict that, in 2040, the volumetric power densities of the stack can reach values approaching 9 kW/l compared to today's 5 kW/l (state of the art). For the optimistic scenario in Table XII, it is assumed that the fuel stack mass density can be reduced to 1/3 of the conservative estimate. This choice must be seen in conjunction with the choice of a very low maximum cell power density set in Section V-H2 compared to the predictions in [38].

An average of the conservative and optimistic parameters is used for the baseline case. Table XII summarizes the parameter choices.

I. PTW and End-to-End Efficiency for the System

The PTW of the total system is defined as the ratio of maximum propeller power (4.1 MW) to the total system weight, where

$$\mathrm{PTW_{tot}} = \frac{P_{\mathrm{prop,max}}}{m_{\mathrm{tot}}}. \tag{35}$$

Moreover, the average end-to-end efficiency is defined as the ratio of total energy drawn from the fuel tank to the total energy delivered to the propeller over the entire mission, yielding

$$\eta_{\mathrm{tot,avg}} = \frac{\int_0^{\mathrm{e.o.m.}} P_{\mathrm{H_2,HHV}}(t)\,dt}{\int_0^{\mathrm{e.o.m.}} P_{\mathrm{prop}}(t)\,dt}. \tag{36}$$

Here, e.o.m. is the time at the end of mission.

VI. ANALYSIS AND MAIN RESULTS

This section describes how all the results were obtained before presenting the main results and analyzing their implications.

A. Simulation Model

The model framework established in Section V has been implemented in a simulation model that calculates all power and loss flows, as well as hydrogen temperatures and so on, through all mission phases. The timestep between each calculation point is 2.5 s.

The simulation model has been implemented in the MATLAB numerical environment. In the following, the model implementation will be described from the bottom and up, starting with the *Power Model* that calculates the power, heat loss, and so on (see green output rectangle in Fig. 9) for all components in the system at any given operating point. Next comes the *Mission Iteration* module, which calls on the *Power Model* at each timestep during the mission profile. Finally, the sequence of the *Simulation Steps* is explained.

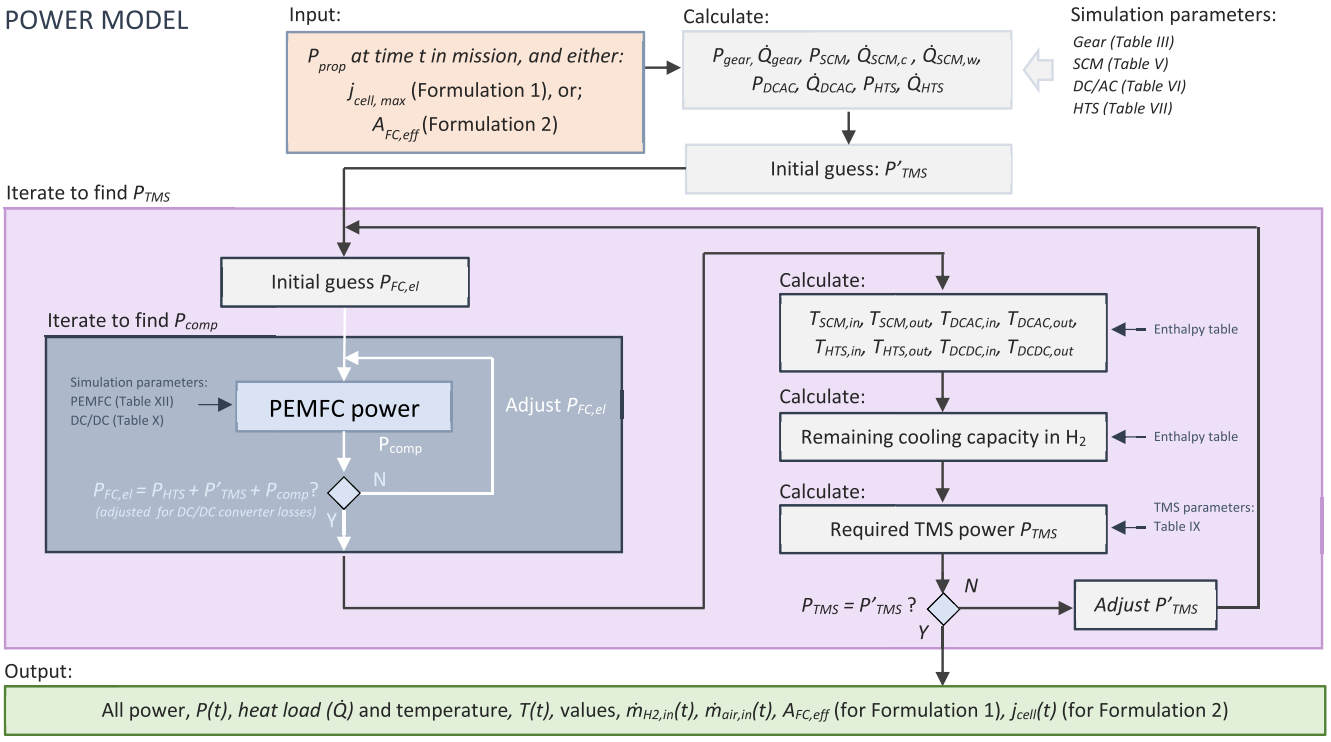

Fig. 9. Flowchart of the power model.

1) Power Model: The flowchart for the *Power Model* is depicted in Fig. 9. It takes the propeller power at each timestep as an input variable. It also takes either a specified maximum FC current density, $j_{\text{cell,max}}$, or a specified total effective fuel cell area, $A_{\text{FC,eff}}$, as an input parameter. The model formulation is slightly different for the two cases, hence the two alternative formulations *Formulation 1* and *Formulation 2*.

As mentioned at the beginning of Section V, the power rating and heat loads of the components are calculated in the upstream direction. This is trivial for the gear, the SCM, the dc/ac inverter, and the HTS cables. These values are calculated directly, as can be seen in Fig. 9.

The TMS and the FC compressor power cannot be determined directly because their power requirements are dependent on the operation point of the PEMFC and vice versa. In the *Power Model*, this has been solved by introducing two iteration loops. The outer loop starts with an initial guess, P'_{TMS}, and uses this to calculate the actual TMS power demand, P_{TMS}. P'_{TMS} is then adjusted until the two values come out equal within a specified tolerance ($\pm$100 W).

The inner loop does the same for the compressor power, P_{comp}. The PEMFC output power, $P_{\text{FC,el}}$, is adjusted until its power balances with the load (within $\pm$100 W).

Since the dc/dc converter lies between the PEMFC, the compressor, and TMS, its efficiency is accounted for in these calculations.

2) Mission Iteration: The *Power Model* is run for each timestep over the full mission. The *Mission Iteration* sequence depicted in Fig. 10 calls on the *Power Model* to do this. *Mission Iteration* outputs all power, heat load, mass flow, and temperature values at each time instance. The maximum power and mass flow values required to size the components are also collected in the sequence.

3) Simulation Steps: Fig. 11 outlines the overall sequence followed for each simulation case.

The first step is to specify the input parameters for the simulation (see Table XIII for further details).

The second step is to determine what $j_{\text{cell,max}}$ value yields the lowest total system mass, m_{tot}. In this step, all component masses are calculated for a range of $j_{\text{cell,max}}$ input values. The maximum PEMFC power, $P_{\text{FC,el}}$, occurs at $t = 60$ s. This operation is used to determine the required effective FC area, $A_{\text{FC,eff}}$, for each value of $j_{\text{cell,max}}$. *Formulation 1* of the *Mission Model* is used for this purpose. Once $A_{\text{FC,eff}}$ has been determined, each mission point is evaluated by calling *Mission Iteration*. The breakdown of the component masses are stored for each value of $j_{\text{cell,max}}$.

The third step is to evaluate the resulting component masses as a function of $j_{\text{cell,max}}$ and identify the value of $A_{\text{FC,eff}}$ that yields the minimum system mass. The corresponding $A_{\text{FC,eff}}$ is then used as an input to step four.

In the fourth and last step, *Mission Iteration* is run with the FC cell area, $A_{\text{FC,eff}}$, which yielded minimum mass in the previous step to produce all required output values for further evaluation.

B. Simulation Cases

Table XIII lists all the simulation cases that have been analyzed. For each of the main scenarios, *Baseline (B)*, *Optimistic (O)*, and *Conservative (C)*, four different constellations are simulated. The differences lie in whether the system comprises a gearbox or not, and whether the hydrogen enters the cooling

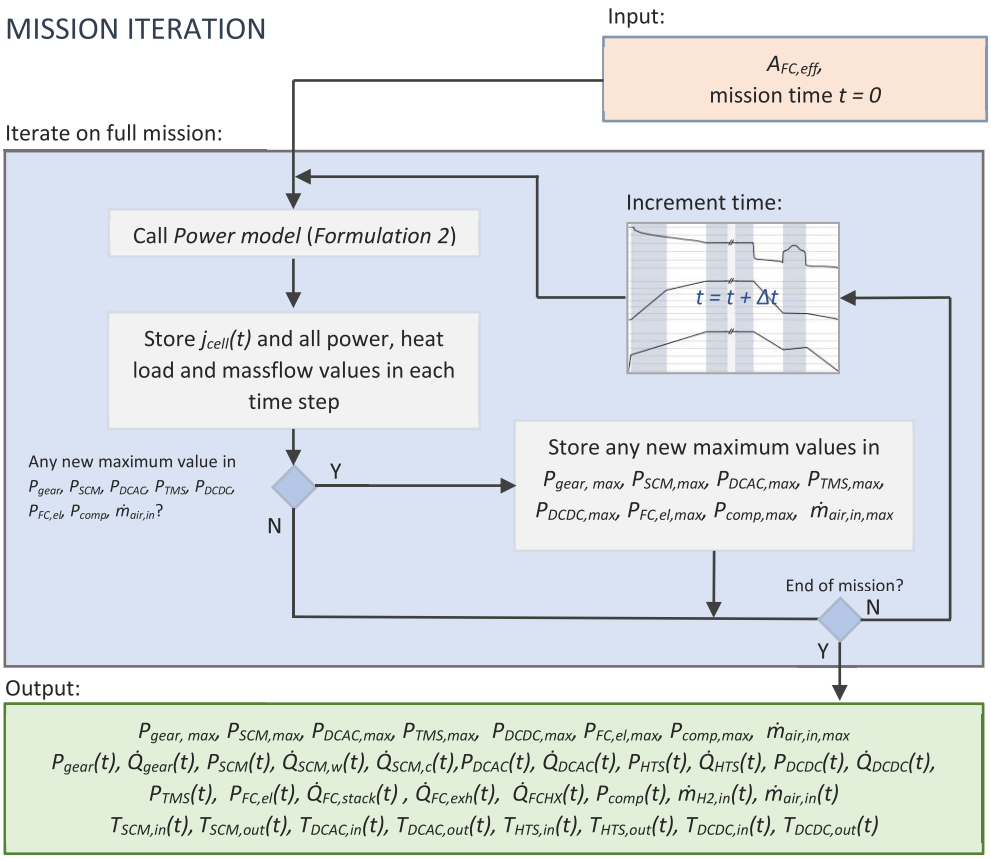

Fig. 10. Flowchart of Mission Iteration. All variables that are given as a function of time t in the green output rectangle are calculated for each timestep. These include power, heat loss, mass flows, and hydrogen temperatures. The time resolution is $\Delta t = 2.5$ s.

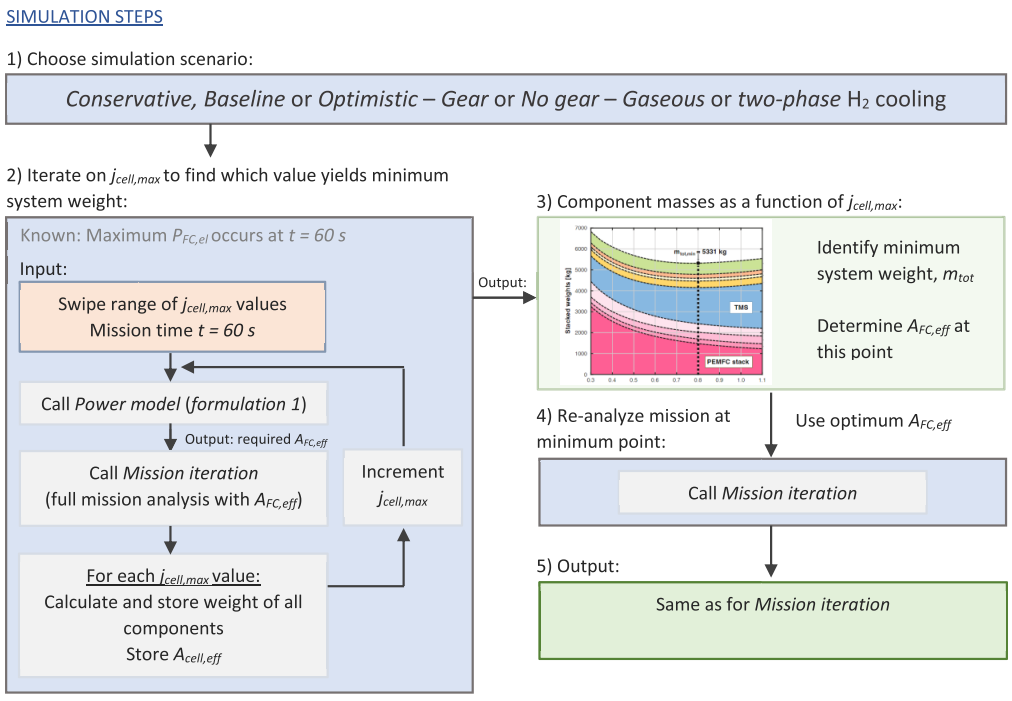

Fig. 11. Flowchart of simulation steps.

circuit as saturated vapor at 22.164 K (gaseous cooling) or fully liquid at 20 K (two-phase cooling).

A sensitivity study, *S1*, has also been performed. The study is centered on the baseline values. Each of the SCM parameters is varied individually, while all other parameters are kept at their baseline values.

Simulation cases *B1* and *B2* (highlighted in blue) are used as comprehensive case studies in Section VI-C. The same

TABLE XIII
SIMULATION MATRIX

Study	Case No.	Baseline Param.	Optimistic Param.	Conservative Param.	Direct Drive	Gear	Gaseous Cooling	Two-Phase Cooling
Baseline Scenario	B1	X			X		X	
	B2	X			X			X
	B3	X				X	X	
	B4	X				X		X
Optimistic Scenario	O1		X		X		X	
	O2		X		X			X
	O3		X			X	X	
	O4		X			X		X
Conservative Scenario	C1			X	X		X	
	C2			X	X			X
	C3			X		X	X	
	C4			X		X		X
Sensitivity Study, SCM	S1	X			X	X	X	

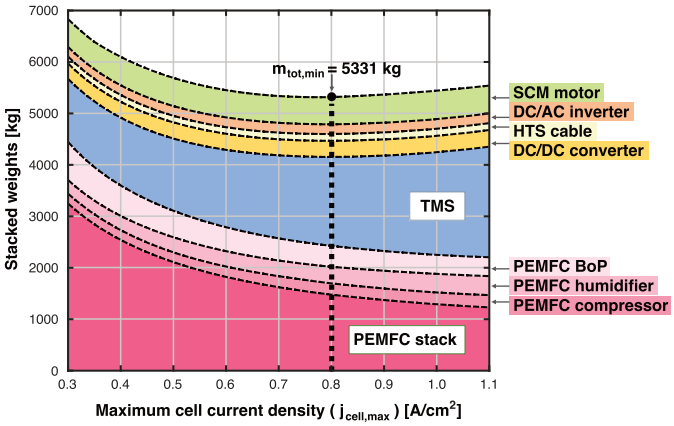

Fig. 12. Case B1: system mass versus maximum PEMFC current density $j_{\text{cell,max}}$. The minimum total system mass occurs at $j_{\text{cell,max}} = 0.8$ A/cm^2. Fig. 13(b) shows how the PEMFC current density of the mass-optimized system peaks at 0.8 A/cm^2.

approach is subsequently applied to all the other scenarios, but then only the main results are reported.

C. Case Study, Simulation Cases B1 and B2

The simulation steps described in the flowchart in Fig. 11 have been followed. After the input parameters have been defined, the value for $j_{\text{cell,max}}$ that minimizes the total system mass can be found. Fig. 12 shows the resulting total system mass for simulation case *B1* for $j_{\text{cell,max}}$ values ranging from 0.3–1.1 A/cm^2. A minimum total system mass of $m_{\text{tot}} = 5331$ kg is achieved for $j_{\text{cell,max}} = 0.8$ A/cm^2. For this point, the total effective FC area is $A_{\text{FC,eff}} = 894$ m^2.

When two-phase cooling is employed instead (case *B2*), a very similar result is obtained. Here, the minimum total system mass of 5316 kg is achieved for $j_{\text{cell,max}} = 0.8$ A/cm^2.

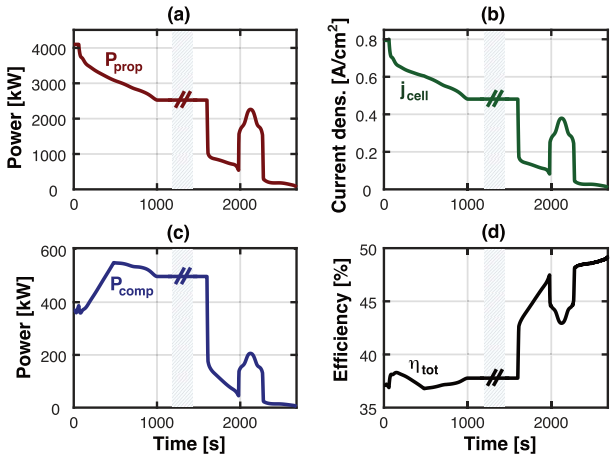

Fig. 13. Case B1 over the entire mission, where the results from case B2 are practically identical. (a) Propeller power (P_{prop}). (b) Fuel cell current density (j_{cell}). (c) Compressor power (P_{comp}). (d) Total system efficiency (η_{tot}).

Fig. 13 plots the instantaneous values for the output power (P_{prop}), fuel cell current density (j_{cell}), compressor power (P_{comp}), and total end-to-end efficiency (η_{tot}) over the entire mission. The results are from simulation case *B1*. The results from simulation case *B2* are practically identical and have been omitted.

In Fig. 13(b), the maximum current density occurs at $t = 60$ s with $j_{\text{cell,max}} = 0.8$ A/cm^2. The compressor power in Fig. 13(c) peaks at 550 kW. This occurs at $t = 480$ s (top of initial climb). This is an important observation since it demonstrates how the sizing of the compressor is not only dependent on the system's power but also on the ambient air pressure. Finally, it is observed in Fig. 13(d) that the total end-to-end system efficiency depends on both propulsive power and altitude. The average end-to-end efficiency, $\eta_{\text{tot,avg}}$, calculated from (36) is 38.54%. When two-phase cooling is employed (case *B2*), the average end-to-end efficiency is practically identical (38.56%).

Fig. 14 gives a detailed account of the power and heat flow in the system at maximum power and cruise power in case *B1*. The PEMFC operates at a higher efficiency at cruise power compared to maximum power, but this has little actual impact on the end-to-end efficiency due to the higher compressor power at cruise altitude.

The power and heat flow in case *B2* are very similar to case *B1* (see Fig. 14). The only notable difference is that a larger fraction of the heat load from the FC stack is rejected to the hydrogen in case *B2*. This is due to the fact that the total cooling capacity of the hydrogen is larger when two-phase cooling is employed. In case *B2*, the normalized heat loads from the FC stack rejected to hydrogen are 2.2% and 2.1% at maximum and cruise powers, respectively, compared to 1.9% and 1.8% in case *B1*.

In the results presented thus far, the difference between case *B1* and *B2* has been negligible or very small. This is not the case for the hydrogen temperatures, where the initial state of the hydrogen in the cryogenic cooling circuit makes a large difference.

Fig. 15(a) shows how the temperature over the cryogenic components vary over the mission in case *B1* when the

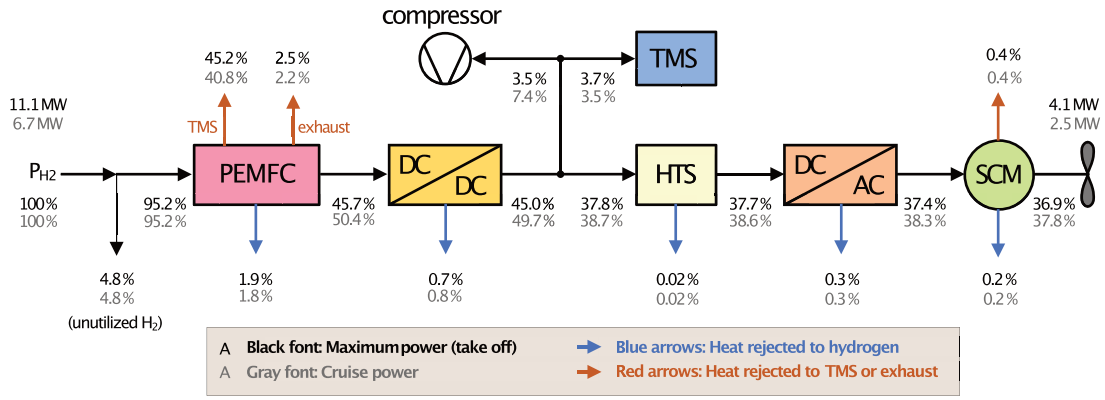

Fig. 14. Case B1: detailed power and heat flow at maximum power and cruise power. All values are normalized to P_{H_2}.

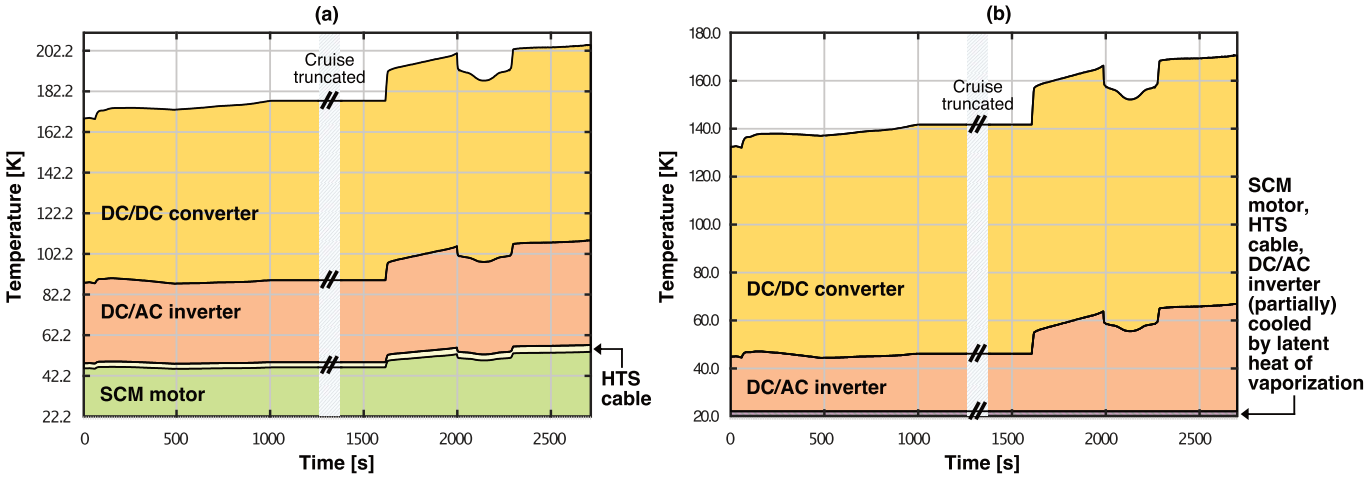

Fig. 15. Hydrogen temperature profile over mission. (a) Gaseous H_2 cooling (case *B1*). (b) Two-phase H_2 cooling (case *B2*).

hydrogen enters the cooling circuit as saturated vapor (T = 22.164 K). Fig. 15(b) shows the same profile for case *B2* when the hydrogen enters the cooling circuit as a liquid at 20 K.

A central observation from Fig. 15 is that the maximum hydrogen temperatures occur at the end of the mission when the system operates at low power. At full power, the hydrogen temperatures are near their minimum values. This relationship is mainly attributed to the PEMFC efficiency curve in Fig. 8. Since the PEMFC efficiency decreases with increasing power, the fuel cell will consume more hydrogen fuel per produced megawatt under the high-power operation. This results in an increase in the hydrogen mass-flow rate ($\dot{m}_{H_2,in}$) relative to the losses produced in the cryogenic cooling circuit, which means that the cryogenic cooling capacity increases at higher propulsive power levels. Consequently, the shape of the temperature profiles in Fig. 15 is nearly identical to the shape of the system efficiency curve in Fig. 13(d). The slight mismatch between the two profiles can mainly be attributed to the compressor power profile not being proportional to the propulsive power [see Fig. 13(c)] but also to a much smaller degree that the heat capacity of hydrogen is not constant over the temperature range.

The hydrogen temperature over the superconducting components has maximum values of $T_{SCM,max}$ = 54.0 K and $T_{HTS,max}$ = 57.3 K. With this cooling arrangement, it is, therefore, not possible to utilize MgB_2 conductors in the SCM since the limiting temperature of 25 K is exceeded (cf. Table I). By using REBCO instead, it is possible to stay within the defined maximum allowable operating temperatures of 60 K and 77 K for the SCM and HTS cables, respectively.

The maximum hydrogen temperature in the dc/ac inverter, $T_{DCAC,max}$, is 108.8 K. This is within the 110 K temperature limit defined in Table I. The temperature in the dc/dc converter experiences a maximum temperature $T_{DCDC,max}$ = 204.9 K and, thus, exceeds the 110 K limit set for the CPE.

In Fig. 15(b), hydrogen enters the cooling circuit fully liquid at 20 K. Due to the high latent heat of vaporization (438 kJ/kg), the hydrogen absorbs a substantial amount of heat during the phase change at T = 22.164 K. Both the SCM and the HTS cables operate at saturation temperature (22.164 K) through the entire mission, which means that either MgB_2 or REBCO is possible option for the SCM in this arrangement. At $T_{DCAC,max}$ = 66.9 K, the dc/ac inverter is well within its 110 K limit, whereas the dc/dc converter falls outside with $T_{DCDC,max}$ = 170.6 K.

D. Compilation of Simulation Results From Cases B, O, and C

1) Performance Metrics: Tables XIV–XVI summarizes the simulation results from the Baseline, Optimistic, and Conservative scenarios.

TABLE XIV

PERFORMANCE METRICS, BASELINE SCENARIO (B), $j_{\text{cell,max}} = 0.8$

		Direct drive (n_{SCM} = 1200 rpm)		With gear (n_{SCM} = 3500 rpm)	
		B1	B2	B3	B4
Metric	Unit	Gaseous cooling	Two-phase cooling	Gaseous cooling	Two-phase cooling
m_{tot}	kg	5331	5316	5178	5162
PTW_{tot}	kW/kg	0.77	0.77	0.79	0.79
$\eta_{tot,avg}$	%	38.54	38.56	38.12	38.15
$T_{SCM,max}$	K	54.0	22.2	53.9	22.2
$T_{HTS,max}$	K	57.3	22.2	57.3	22.2
$T_{DCAC,max}$	K	108.8	66.9	108.7	66.8
$T_{DCDC,max}$	K	204.9	170.6	204.9	170.5

TABLE XV

PERFORMANCE METRICS, OPTIMISTIC SCENARIO (O), $j_{\text{cell,max}} = 0.9$

		Direct drive (n_{SCM} = 1200 rpm)		With gear (n_{SCM} = 3500 rpm)	
		O1	O2	O3	O4
Metric	Unit	Gaseous cooling	Two-phase cooling	Gaseous cooling	Two-phase cooling
m_{tot}	kg	2625	2618	2514	2508
PTW_{tot}	kW/kg	1.56	1.57	1.63	1.63
$\eta_{tot,avg}$	%	45.36	45.38	45.13	45.14
$T_{SCM,max}$	K	28.7	22.2	28.8	22.2
$T_{HTS,max}$	K	29.4	22.2	29.5	22.2
$T_{DCAC,max}$	K	45.2	22.2	45.3	22.2
$T_{DCDC,max}$	K	123.7	83.2	123.9	83.2

TABLE XVI

PERFORMANCE METRICS, CONSERVATIVE SCENARIO (C), $j_{\text{cell,max}} = 0.5$

		Direct drive (n_{SCM} = 1200 rpm)		With gear (n_{SCM} = 3500 rpm)	
		C1	C2	C3	C4
Metric	Unit	Gaseous cooling	Two-phase cooling	Gaseous cooling	Two-phase cooling
m_{tot}	kg	14033	13975	13771	13710
PTW_{tot}	kW/kg	0.29	0.29	0.30	0.30
$\eta_{tot,avg}$	%	33.13	33.18	32.56	32.61
$T_{SCM,max}$	K	78.4	35.1	78.3	35.0
$T_{HTS,max}$	K	84.2	41.0	84.1	40.8
$T_{DCAC,max}$	K	151.1	113.1	150.8	112.9
$T_{DCDC,max}$	K	265.7	232.7	265.5	232.5

When evaluated against the performance targets set for the study (see Table I), all the Conservative scenarios fail to meet the majority of the defined targets. The situation is more promising for the Baseline and Optimistic scenarios. The matrix in Table XVII summarizes the targets met for each case.

Only cases *O2* and *O4* satisfy all the defined target limits. These are the Optimistic cases where two-phase hydrogen cooling is employed. These are also the only two cases where the maximum hydrogen temperature in the dc/dc converter, $T_{\text{DCDC,max}}$, does not exceed the 110 K limit during the mission.

2) Distribution of Component Masses: Fig. 16 shows the relative mass distribution in the system for the three scenarios. Only the gaseous cooling cases are included in the figure since changing to two-phase hydrogen cooling hardly impacts the component weights.

The TMS and the FC stack are the two dominating components in all scenarios. In the Optimistic scenario, the electrical components comprise 25%–30% of the total system mass compared to 12%–16% for the Conservative scenario.

TABLE XVII

MATRIX OF TARGETS MET FOR THE BASELINE AND OPTIMISTIC SCENARIOS. THE TARGET VALUES COME FROM TABLE I. EACH CASE NO. IS DESCRIBED IN TABLE XIII

	Target					
Case No.	$PTW_{tot} > 1$	$T_{SCM,max} < 25$ K	$T_{SCM,max} < 60$ K	$T_{HTS,max} < 77$ K	$T_{DCAC,max} < 110$ K	$T_{DCDC,max} < 110$ K
B1			X	X	X	
B2		X	X	X	X	
B3			X	X	X	
B4		X	X	X	X	
O1	X		X	X	X	
O2	X	X	X	X	X	X
O3	X		X	X	X	
O4	X	X	X	X	X	X

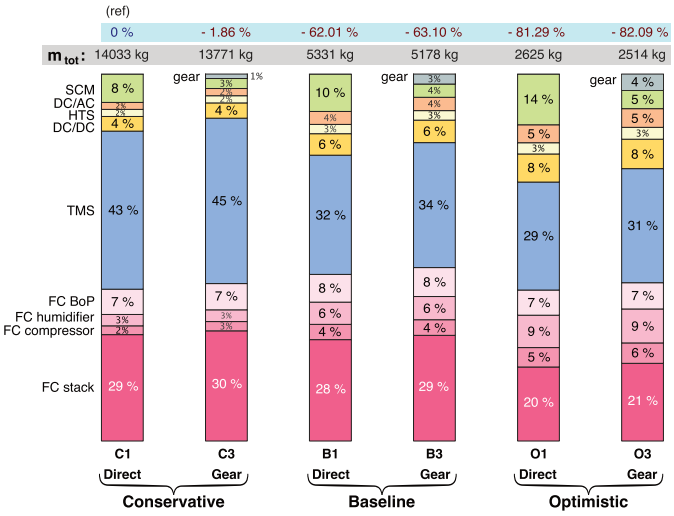

Fig. 16. Mass distribution for simulation cases with gaseous hydrogen cooling. Two-phase hydrogen cooling yields nearly identical results.

E. Case S1: Sensitivity to SCM Parameters

It is of interest to see how the SCM parameters impact the total performance of the cryoelectric architecture. Therefore, a sensitivity analysis is performed around the Baseline *B1* case. Here, each of the parameters from Table V is varied separately, while all the remaining parameters are kept at their Baseline values. Table XVIII summarizes the parameter variations, where reference values from case *B1* are written in boldface.

Fig. 17 shows the impact of varying the SCM parameters individually. Changes in PTW_{tot}, η_{tot}, and $T_{\text{SCM,max}}$ are shown in each of the three plots. The TTW ratio has been excluded from plots (b) and (c) since it has no impact on the outcome.

The main observations from the plot are that the only factors that have any significant impact on the PTW of the total

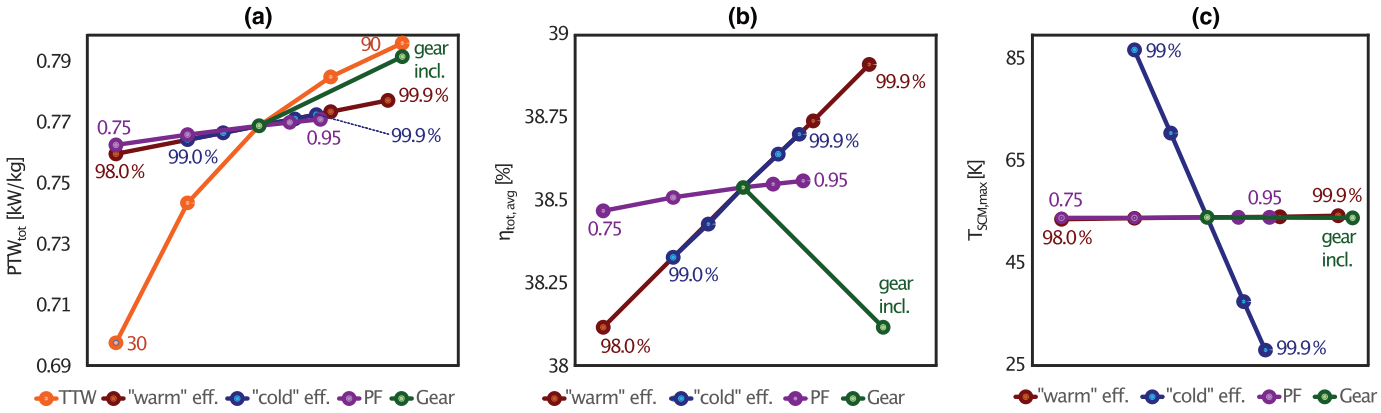

Fig. 17. SCM parameters' impact on (a) PTW_{tot}, (b) $\eta_{tot,avg}$, and (c) $T_{SCM,max}$.

TABLE XVIII
SCM PARAMETER VARIATION IN SENSITIVITY STUDY S1

Parameter	Values
TTW_{SCM} [Nm/kg]	30, 45, **60**, 75, 90
$\eta_{SCM,c}$ [%]	99.00, 99.25, **99.50**, 99.75, 99.90
$\eta_{SCM,w}$ [%]	98.00, 98.50, **99.00**, 99.75, 99.90
PF_{SCM} [-]	0.75, 0.82, **0.89**, 0.92, 0.95
Gear	**No gear**, Gear included

system, PTW_{tot}, are the torque density of the SCM, TTW_{SCM}, and whether a gear is used between the SCM and the propeller.

The average total efficiency of the system [plot (b)], $\eta_{tot,avg}$, is hardly impacted by the power factor of the motor, whereas the gear, and the cold and warm efficiencies, $\eta_{SCM,c}$ and $\eta_{SCM,h}$, show some impact. It should be noted that the efficiencies span over a relatively large range in this study. The gain in total average system efficiency is approximately 0.4 percentage point for each percentage point improvement in $\eta_{SCM,c}$ or $\eta_{SCM,w}$.

In this case (gaseous cooling), the maximum hydrogen temperature, $T_{SMC,max}$, in the SCM is highly dependent on the SCM's cold efficiency. This can be seen in plot (c). $T_{SMC,max}$ is reduced by approximately 65 K per percentage point improvement in $\eta_{SCM,c}$. Furthermore, $T_{SMC,max}$ is practically insensitive to changes in the other parameters.

VII. OUTLINE OF FURTHER RESEARCH ITEMS

This study has been premised on a set of simplifications. These include having the PEMFC as the single source of electrical power in the architecture, and assuming that all useful output power is consumed by the propulsion motor(s). Also, the mission profile does not include taxiing or prolonged periods of standstill. The purpose of this section is to provide an outline of some key aspects that have not been covered in this study on account of said limitations.

A. PEMFC in Combination With Batteries

The PEMFC responds slowly to load changes. It is, therefore, likely that the architecture in Fig. 1 needs to be supplemented with a faster responding secondary energy source in order to improve the transient behavior of the system. Despite having a rather low energy density, a properly dimensioned battery bank can be an attractive alternative. In addition to providing transient power, one could go further and dimension the battery bank to also limit the peak load of the fuel cell, as shown in Fig. 18(a). This will reduce the weight of the PEMFC and the TMS at the cost of added battery weight to fill the power and energy gap. Finding an optimum power split in a hybrid-source system requires careful analysis, and Fig. 18(a) is only intended as an illustrative example.

Fig. 18(b) illustrates an undesired consequence of using batteries to shave off some of the peak power from the PEMFC. The hydrogen mass flow in the cooling circuit is reduced at the high-power operation compared to architecture with PEMFC only. This leads to a reduction in the cryogenic cooling capacity, which can clearly be seen by comparing the temperature profiles in Fig. 18(b) with those of Fig. 15(a). A similar reduction in cooling capacity can also occur during transient load situations, and it will be important to model these mechanisms accurately in more detailed studies.

B. Superconducting Magnetic Energy Storage

An alternative, or supplement, to a battery pack could be superconducting magnetic energy storage (SMES). This energy storage technology is frequently mentioned in conjunction with cryoelectric aircraft architectures [8]. It is worth investigating if synergies can be obtained by combining SMES with the proposed architecture and also possibly with batteries.

C. Decoupling Between Hydrogen Consumption and Cryogenic Cooling

This study has been limited to analyzing a system where the cryogenic cooling capacity is directly coupled to the hydrogen consumption in the PEMFC. From the discussion under Section VII-A, it is clear that some decoupling can be required to ensure sufficient cryogenic cooling at all operation modes. This will also include operation modes not included in the mission profile (see Fig. 2), such as taxiing, where cooling must be maintained at low power.

It may be necessary to add cryocooler(s) in the cooling circuit to achieve the necessary level of decoupling. However,

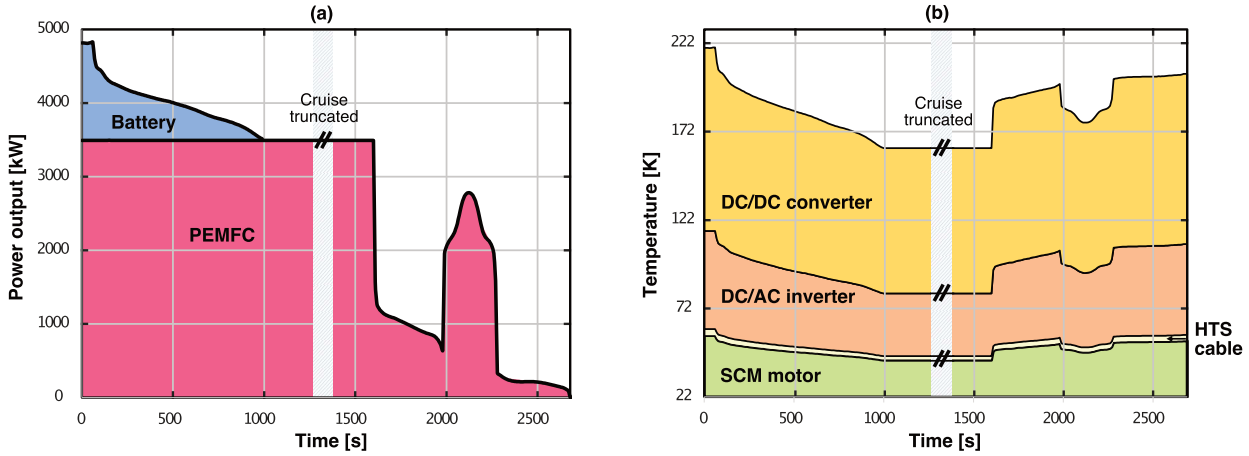

Fig. 18. PEMFC in combination with a battery bank. (a) Power sharing between the PEMFC and the battery bank. (b) Hydrogen temperatures over the duration of the mission. The temperature profiles are based on the results from a nonoptimized system with input parameters from case *B1*.

since cryocoolers are heavy and inefficient, it will be important to explore ways to minimize the required capacity. To this end, deigning the dc/dc converter for noncryogenic operating temperatures could be a beneficial option since it will increase the margins in the cooling system and, thereby, reduce the need for cryocooler(s). Second, decoupling could also be achieved by actively controlling the stoichiometric ratio $\lambda_{H_2,net}$. Since this ratio determines the amount of excess hydrogen that is fed into the PEMFC, it can potentially be controlled actively to increase the cryogenic cooling capacity. This, of course, means using a small part of the stored hydrogen fuel as a once-through cryogen that eventually goes to waste. It could, nevertheless, turn out to be a cost-effective way to limit the need for cryocoolers.

VIII. Conclusion

This article has investigated the feasibility of using liquid hydrogen (LH_2) fuel directly for cryogenic cooling of superconductors and other components operating at cryogenic temperatures in a next-generation PEMFC-powered aircraft. Furthermore, it has been investigated if system power densities of 1 kW/kg or better are achievable for an architecture that constitutes the components depicted in Fig. 1.

As of today, the technology has investigated low TRL, and the performance parameters have, therefore, been projected to three different 2035 scenarios—a conservative, a baseline, and an optimistic scenario.

When the optimistic parameter sets are applied, the total system power density exceeds 1.5 kW/kg (PTW_{tot}; see Table XV). For the baseline and conservative scenarios, the power density values are ∼0.75 and ∼0.30 kW/kg, respectively (see Tables XIV and XVI). The added mass from protection systems, redundancy requirements, battery bank, and so on has not been considered in this study (see Section II). It is, therefore, clear that the technology development toward 2035 must move well beyond the baseline scenario to meet the goal of 1-kW/kg total system power density.

Under the simulated conditions, it is also possible to keep each component within the defined cryogenic temperature limits. The dc/dc converter has proven most difficult to maintain within the temperature limit of 110 K. This is because it has been placed at the warm end of the cryogenic cooling loop in the simulated configurations. For the dc/dc converter to be properly cooled, it is required that the efficiencies of the cryogenic components approach the values set in the optimistic scenario, and the two-phase hydrogen cooling is employed. All other components are sufficiently cooled in the baseline and optimistic scenarios, but some configurations require that REBCO superconductors are to be used in the SCM since the target limit for MgB_2 is exceeded. As discussed in Section VII, power sharing between the PEMFC and a battery pack can have a significant impact on the hydrogen temperatures, both for transient and more static load variations. These aspects are not captured by the models developed for this study and require further investigation.

In addition to the results mentioned above, it has also been shown how the hydrogen temperatures reach maximum values at the final stage of the mission where the system power is low. Conversely, the temperatures are very near their minimum values at peak load. As discussed under Section VI-C, cryogenic cooling improves with falling PEMFC efficiency.

In addition to the need for future work outlined in Section VII, the authors have identified the following need for model improvements.

1) The analysis performed in this study has been quasi-static. The time-dependent results are obtained from analyzing a chain of equilibrium states. It will, therefore, be important to further develop models to accurately analyze the system's transient behavior as well.
2) The component models employed in this study are limited in scope. They should be refined to include transient behavior, efficiency variations, and so on. Moreover, heat leak in the cryogenic circuit has also been neglected in this study, and should be investigated in future studies.
3) The TMS model has been based on coarse approximations. Given its impact on the overall system, it should be a priority to establish a more accurate basis for determining the size and power consumption of the TMS.

REFERENCES

[1] J. K. Noland, "Hydrogen electric airplanes: A disruptive technological path to clean up the aviation sector," *IEEE Electrific. Mag.*, vol. 9, no. 1, pp. 92–102, Mar. 2021.

[2] Y. Tao, J. Qiu, S. Lai, X. Zhang, and G. Wang, "Collaborative planning for electricity distribution network and transportation system considering hydrogen fuel cell vehicles," *IEEE Trans. Transport. Electrific.*, vol. 6, no. 3, pp. 1211–1225, Sep. 2020.

[3] C. Sabillon, B. N. Singh, and B. Venkatesh, "Technoeconomic models for the optimal inclusion of hydrogen trains in electricity markets," *IEEE Trans. Transport. Electrific.*, vol. 5, no. 3, pp. 758–768, Sep. 2019.

[4] A. Haxhiu, A. Abdelhakim, S. Kanerva, and J. Bogen, "Electric power integration schemes of the hybrid fuel cells and batteries-fed marine vessels—An overview," *IEEE Trans. Transport. Electrific.*, vol. 8, no. 2, pp. 1885–1905, Jun. 2022.

[5] T. C. Cano *et al.*, "Future of electrical aircraft energy power systems: An architecture review," *IEEE Trans. Transport. Electrific.*, vol. 7, no. 3, pp. 1915–1929, Sep. 2021.

[6] E. Sayed *et al.*, "Review of electric machines in more-/hybrid-/turbo-electric aircraft," *IEEE Trans. Transport. Electrific.*, vol. 7, no. 4, pp. 2976–3005, Dec. 2021.

[7] C. E. Jones *et al.*, "A route to sustainable aviation: A roadmap for the realization of aircraft components with electrical and structural multifunctionality," *IEEE Trans. Transport. Electrific.*, vol. 7, no. 4, pp. 3032–3049, Dec. 2021.

[8] C. E. Jones, P. J. Norman, S. J. Galloway, M. J. Armstrong, and A. M. Bollman, "Comparison of candidate architectures for future distributed propulsion aircraft," *IEEE Trans. Appl. Supercond.*, vol. 26, no. 6, pp. 1–9, Sep. 2016.

[9] M. Schröder, F. Becker, J. Kallo, and C. Gentner, "Optimal operating conditions of PEM fuel cells in commercial aircraft," *Int. J. Hydrogen Energy*, vol. 46, no. 66, pp. 33218–33240, Sep. 2021.

[10] M. Boll *et al.*, "A holistic system approach for short range passenger aircraft with cryogenic propulsion system," *Superconductor Sci. Technol.*, vol. 33, no. 4, Apr. 2020, Art. no. 044014.

[11] F. Berg, J. Palmer, P. Miller, M. Husband, and G. Dodds, "HTS electrical system for a distributed propulsion aircraft," *IEEE Trans. Appl. Supercond.*, vol. 25, no. 3, pp. 1–5, Jun. 2015.

[12] M. Filipenko *et al.*, "Concept design of a high power superconducting generator for future hybrid-electric aircraft," *Superconductor Sci. Technol.*, vol. 33, no. 5, May 2020, Art. no. 054002.

[13] P. Cheetham, I. Barnola, C. Kim, and S. Pamidi, "Exploring options for integrated cryogenic circulation loop of superconducting power devices on electric aircraft," in *Proc. AIAA Propuls. Energy Forum*, Aug. 2019, pp. 1–8.

[14] C. Wright Electric. (2021). *Wright Spirit Energy Storage Discussion Paper*. [Online]. Available: https://docsend.com/view/faijiijzkvqdccjg

[15] B. Jux, S. Foitzik, and M. Doppelbauer, "A standard mission profile for hybrid-electric regional aircraft based on web flight data," in *Proc. IEEE Int. Conf. Power Electron., Drives Energy Syst. (PEDES)*, Dec. 2018, pp. 1–6.

[16] M. Cavcar, "The international standard atmosphere (ISA)," *Anadolu Univ., Turkey*, vol. 30, no. 9, pp. 1–6, 2000.

[17] P. D. A. S. (PDAS). (2021). *The US Defense Department Non-Standard Atmospheres*. [Online]. Available: https://www.pdas.com/milstd210.html

[18] J. M. Rheaume, M. MacDonald, and C. E. Lents, "Commercial hybrid electric aircraft thermal management system design, simulation, and operation improvements," in *Proc. AIAA Propuls. Energy Forum*, Aug. 2019, pp. 1–23.

[19] E. W. Lemmon, M. O. McLinden, and D. G. Friend, "Thermophysical properties of fluid systems," in *NIST Chemistry Webbook, NIST Standard Reference Database Number 69*, P. J. Linstrom and W.G. Mallard, Eds. Gaithersburg MD, USA: NIST, 1998, doi: 10.18434/T4D303.

[20] G. V. Brown *et al.*, "NASA Glenn research center program in high power density motors for aeropropulsion," Nat. Aeronaut. Space Admin. Cleveland, Cleveland, OH, USA, Tech. Rep.NASA/TM-2005-213800, 2005.

[21] N. E. Anderson, S. H. Loewenthal, and J. D. Black, "An analytical method to predict efficiency of aircraft gearboxes," NASA Lewis Research Center, Cleveland, Oh, USA, Tech. Rep. Usaavscom-TR-84-C-8, 1986.

[22] R. Jansen, C. Bowman, and A. Jankovsky, "Sizing power components of an electrically driven tail cone thruster and a range extender," in *Proc. 16th AIAA Aviation Technol., Integr., Oper. Conf.*, Jun. 2016, p. 3766.

[23] R. Jansen, C. Bowman, A. Jankovsky, R. Dyson, and J. Felder, "Overview of NASA electrified aircraft propulsion (EAP) research for large subsonic transports," in *53rd AIAA/SAE/ASEE joint Propuls. Conf.*, vol. 2017, p. 4701.

[24] H. D. Kim, G. V. Brown, and J. L. Felder, "Distributed turboelectric propulsion for hybrid wing body aircraft," in *Proc. 9th Int. Powered Lift Conf.*,1 London, U.K.: Citeseer, 2008, pp. 1–12.

[25] F. Berg, J. Palmer, P. Miller, and G. Dodds, "HTS system and component targets for a distributed aircraft propulsion system," *IEEE Trans. Appl. Supercond.*, vol. 27, no. 4, pp. 1–7, Jun. 2017.

[26] B. Aigner, M. Nollmann, and E. Stumpf, *Design of a Hybrid Electric Propulsion System Within a Preliminary Aircraft Design Software Environment*. Bonn, Germany: Deutsche Gesellschaft Für Luft-und Raumfahrt-Lilienthal-Oberth eV, 2018.

[27] J. Rheaume and C. E. Lents, "Design and simulation of a commercial hybrid electric aircraft thermal management system," in *Proc. AIAA/IEEE Electr. Aircr. Technol. Symp.*, Jul. 2018, p. 4994.

[28] H. Kellermann, M. Lüdemann, M. Pohl, and M. Hornung, "Design and optimization of ram air–based thermal management systems for hybrid-electric aircraft," *Aerospace*, vol. 8, no. 1, p. 3, Dec. 2020.

[29] J. W. Chapman, S. L. Schnulo, and M. P. Nitzsche, "Development of a thermal management system for electrified aircraft," in *Proc. AIAA Scitech Forum*, Jan. 2020, p. 545.

[30] C. E. Lents, L. W. Hardin, J. Rheaume, and L. Kohlman, "Parallel hybrid gas-electric geared turbofan engine conceptual design and benefits analysis," in *Proc. 52nd AIAA/SAE/ASEE Joint Propuls. Conf.*, Jul. 2016, p. 4610.

[31] H. Kellermann, A. L. Habermann, and M. Hornung, "Assessment of aircraft surface heat exchanger potential," *Aerospace*, vol. 7, no. 1, p. 1, Dec. 2019.

[32] T. Hong, Z. Geng, K. Qi, X. Zhao, J. Ambrosio, and D. Gu, "A wide range unidirectional isolated DC–DC converter for fuel cell electric vehicles," *IEEE Trans. Ind. Electron.*, vol. 68, no. 7, pp. 5932–5943, Jul. 2021.

[33] P. Channegowda, S. Du, P. Kshirsagar, and S. Dwari, "Mega-watt class ultra-high density DC-DC converters for future electric aircraft systems," in *Proc. AIAA Propuls. Energy Forum*, Aug. 2019, pp. 1–11.

[34] M. Warncke, S. Fahlbusch, and K. F. Hoffmann, "DC/DC-converter for fuel cell integration in more electric aircraft applications," in *Proc. 19th Eur. Conf. Power Electron. Appl. (EPE ECCE Eur.)*, Sep. 2017, p. 1.

[35] B. Łukasik, "Turboelectric distributed propulsion system as a future replacement for turbofan engines," in *Turbo Expo: Power for Land, Sea, and Air*, vol. 50770. New York, NY, USA: American Society of Mechanical Engineers, 2017, Art. no. V001T01A017.

[36] F. Barbir, *PEM Fuel Cells: Theory and Practice*. New York, NY, USA: Academic, 2012.

[37] A. Thirkell, "Systems study for fuel cell powered more electric aircraft," Ph.D. dissertation, Dept. Aeronaut. Automot. Eng., Loughborough, U.K., Loughborough Univ., 2021.

[38] K. Jiao *et al.*, "Designing the next generation of proton-exchange membrane fuel cells," *Nature*, vol. 595, pp. 361–369, Jul. 2021.

[39] J. C. Kurnia, A. P. Sasmito, and T. Shamim, "Advances in proton exchange membrane fuel cell with dead-end anode operation: A review," *Appl. Energy*, vol. 252, Oct. 2019, Art. no. 113416.

[40] H. Struchtrup, *Thermodynamics and Energy Conversion*. Cham, Switzerland: Springer, 2014.

[41] A. Lombardi, D. Ferrari, and L. Santos, "Aircraft air inlet design optimization via surrogate-assisted evolutionary computation," in *Proc. Int. Conf. Evol. Multi-Criterion Optim.*, Cham, Switzerland: Springer, 2015, pp. 313–327.

[42] Y. Wang *et al.*, "Thermal management system modeling and simulation of a full-powered fuel cell vehicle," *J. Energy Resour. Technol.*, vol. 142, no. 6, pp. 061304-1-061304-12, Jun. 2020.

Christian Hartmann received the M.Sc. degree in electric power engineering from the Norwegian University of Science and Technology (NTNU), Trondheim, Norway, in 1999. Since 2012, he has been a Senior Researcher with the Institute for Energy Technology, Halden, Norway. He is currently a part-time Ph.D. student with NTNU. The focus of his work is cryoelectric propulsion systems for next-generation aviation.

Jonas Kristiansen Nøland (Senior Member, IEEE) was born in Drammen, Norway, in 1988. He received the M.Sc. degree in electric power engineering from the Chalmers University of Technology, Gothenburg, Sweden, in 2013, and the Ph.D. degree in engineering physics from Uppsala University, Uppsala, Sweden, in 2017.

Since 2018, he has been an Associate Professor with the Department of Electric Power Engineering, Norwegian University of Science and Technology, Trondheim, Norway. His current research interests include excitation systems, improved utilization of electrical machines, high-power machinery for aircraft applications, hyperloop propulsion and levitation, and transportation electrification in general.

Dr. Nøland also serves as an Editor for the IEEE TRANSACTIONS ON ENERGY CONVERSION and an Associate Editor for the IEEE TRANSACTIONS ON INDUSTRIAL ELECTRONICS.

Robert Nilssen received the Dr.Ing. degree from the Norwegian Institute of Technology (NTH), Trondheim, Norway, in 1989.

From 1989 to 1996, he was an Associate Professor with NTH. In that period, he was a Scientific Advisor for SINTEF, Trondheim. Since 1996, he has been a Professor with the Norwegian University of Science and Technology (NTNU), Trondheim, with numerical electromagnetic field calculations as his main responsibility. In that period, he has participated in a series of research projects in which design and optimization have been important. He has been a co-founder of several industrial companies. He has been a Scientific Advisor for several companies and, in particular, for SmartMotor AS, Trondheim, and Rolls-Royce Norway, Trondheim, focusing on marine and aviation applications of permanent magnet machines.

Runar Mellerud received the M.Sc. degree in electrical engineering from the Norwegian University of Science and Technology (NTNU), Trondheim, Norway, in 2021, where he is currently pursuing the Ph.D. degree in superconducting electrical machines for aerospace applications.